

ANALYTICAL EVALUATION OF EFFECTIVE SOLAR SAIL
ATTITUDE CONTROL USING METASURFACES FOR
DEEP SPACE EXPLORATION

by

DYLAN C. ULLERY

SEONGSIN MARGARET KIM, COMMITTEE CHAIR
PATRICK KUNG
ROHAN SOOD

A THESIS

Submitted in partial fulfillment of the requirements for the degree
of Master of Science in the Department of
Electrical and Computer Engineering
in the Graduate School of The
University of Alabama

TUSCALOOSA, ALABAMA

2018

Copyright Dylan C. Ullery 2018
ALL RIGHTS RESERVED

ABSTRACT

We examine the theoretical implications of incorporating metasurfaces on solar sails, and the effect they can have on the forces and torques applied to the sail. This would enable a significant enhancement over state-of-the-art attitude control by demonstrating a novel, propellant-free and low mass approach to induce a roll torque on the sail, which is a current limitation in present state-of-the-art technology. We do so by utilizing anomalous optical reflections from the metasurfaces to generate a net in-plane lateral force. This can lead to a net torque along the roll axis of the sail, in addition to the other spatial movements exhibited by the sail from solar radiation pressure. We characterize this net lateral force as a function of incidence angle. In addition, the influence of the phase gradients and anomalous conversion efficiency characteristics of the metasurfaces are independently considered. The optimum incidence angle that corresponded with the maximum net lateral-to-normal force ratio was found to be -30° for a metasurface exhibiting 75% anomalous conversion efficiency with a phase gradient of $0.71k_0$. Upon comparison with the force and torque plots from current reflection control devices such as those that were utilized on IKAROS, the anomalously reflecting metasurfaces offer a considerable increase in torque along the roll axis. This is important because up until this point, roll control has been a particularly difficult aspect of solar sail attitude control to manipulate without the use of reaction wheels or propellant. The torque along the roll axis can reach values of torque as high as $358 \mu N m$ under ideal conditions.

DEDICATION

This thesis is dedicated to my wife, Alea, and our two wonderful children, Christian and Connor.

LIST OF ABBREVIATIONS AND SYMBOLS

Acronyms:

NASA	National Aeronautic and Space Administration
EM	Electromagnetic
ARM	Anomalously Reflecting Metasurface
RCD	Reflectivity Control Device
IKAROS	Interplanetary Kite-craft Accelerated by Radiation Of the Sun
JAXA	Japanese Aerospace Exploration Agency
NEA	Near-Earth Asteroid
MSFC	Marshall Space Flight Center
ACS	Attitude Control System
AMT	Active Mass Translator
RCS	Reaction Control System
CM	Center of Mass
CP	Center of Pressure
NMP	N-Methyl-2-Pyrrolidone
CVD	Chemical Vapor Deposition
CMOS	Complementary Metal-Oxide-Semiconductor
TMDC	Transition Metal Dichalcogenide
FEM	Finite Element Method

FDTD Finite-Difference Time-Domain

Solar Radiation Model Derivations:

F_τ	Transmission Force
F_γ	Absorption/Emission Force
F_ρ	Total Reflection Force
τ_r	Transmission Coefficient
γ	Absorption/Reflection Coefficient
ρ	Reflection Coefficient
F_{tot}	Total Force on the Solar Sail
f_α	Absorption Force
f_e	Emission Force
p	Momentum
t	Time
E	Energy
\mathbf{n}	Normal Unit Vector
\mathbf{u}	Incident Radiation Unit Vector
\mathbf{t}	Tangential Unit Vector
c	Speed of Light
W	Radiative Flux
θ	Incident Angle
ϵ_f	Front Side Emissivity Coefficient
ϵ_b	Back Side Emissivity Coefficient

σ	Stefan-Boltzmann Constant
T_{eq}	Equilibrium Temperature
B_f	Front Side Lambertian Coefficient
B_b	Back Side Lambertian Coefficient
s	Specular Reflection Coefficient
F_s	Specular Reflection Force
d	Diffuse Reflection Coefficient
F_d	Diffuse Reflection Force
f_i	Incident Force
f_r	Reflection Force
θ	Angle of Observation
ϕ	Clock Angle/Polar Angle
I_{Max}	Max Intensity
$F_{tot,t}$	Total Tangential Force
$F_{tot,n}$	Total Normal Force
P	Maximum Solar Radiation Pressure
S	Solar Sail Surface Area

Electromagnetic Derivations:

E_0	Electric Field Amplitude
ϵ	Electric Permittivity
μ	Magnetic Permeability
η	Wave Impedance

k	Wavenumber
ϵ_0	Free-Space Electric Permittivity
μ_0	Free-Space Magnetic Permeability
η_0	Free-Space Wave Impedance
k_0	Free-Space Wavenumber
n_i	Refractive Index
θ_i	Angle of Incidence
θ_r	Reflection Angle
Φ	Phase Shift
ζ	Constant Phase Gradient
η_{anom}	Anomalous Reflection Conversion Efficiency
\mathbf{f}	Force Density
\mathbf{E}	Electric Field of EM Wave
\mathbf{H}	Magnetic Field of EM Wave
\mathbf{D}	Electric Displacement Field of EM Wave
\mathbf{B}	Magnetic Induction Field of EM Wave
\mathbf{S}	Poynting Vector
$\vec{\mathbf{T}}$	Maxwell Stress Tensor
$\vec{\mathbf{I}}$	Identity Tensor
$L_{x,y}$	Length of Solar Sail Edge
l_x	Length of Metasurface Unit Cell
a	Width of Longest Edge of Metasurface

\mathbf{F}	Force Vector
\mathbf{r}	Position Vector with Respect to Origin
$\boldsymbol{\tau}$	Torque Vector
V	Solar Sail Volume
$\hat{\mathbf{n}}$	Normal Unit Vector
s_{ON}	Specular Reflection Coefficient When Specular Surface is Active
s_{OFF}	Specular Reflection Coefficient When Diffuse Surface is Active
$\boldsymbol{\tau}_{net}$	Net Torque Vector
$\boldsymbol{\tau}_{opt}$	Optimal Vector to Produce Maximum Roll Torque

Other Symbols:

A	Absorption
R	Reflection
T	Transmission
E_F	Fermi Energy
v_F	Fermi Velocity
n	Carrier Density
C	Capacitance
V	Voltage Difference
e	Carrier Charge

ACKNOWLEDGMENTS

I would like to begin by thanking my two main collaborative professors, my adviser, Dr. Seongsin Margaret Kim, and Dr. Patrick Kung. Without their help, I know that I would not have been able to accomplish the things I have done over the last two years, and I am very grateful to have had the opportunity to learn from them. By allowing me to be a part of their research group, I was immersed in a collaborative and engaging environment that was crucial to my success as a graduate student. In that sense, I would also like to thank all of my fellow group members for all of the help and discussion in both research and classwork.

Next, I would like to thank Dr. Rohan Sood, from my thesis committee. As a part of the Aerospace Engineering Department, he provided an alternative perspective from those inside the Electrical Engineering Department that proved to be very important to the topic.

Next, I am forever grateful to my mom and dad. From the start, they have encouraged me to pursue and improve myself in subjects relating to both writing and science/technology. I am very thankful for everything they have done for me.

Finally, I would like to thank my wife, Alea, for supporting me as I pursued my Master's degree. There were many times where juggling the responsibility of raising our two sons with the graduate school workload seemed insurmountable, but Alea was always there to offer limitless encouragement and support. She is the backbone behind our family and she is truly a most wonderful and loving mother to our sons.

Financial support was provided by the ASGC NASA Training Grant #NNX15AJ18H.

CONTENTS

ABSTRACT.....	ii
DEDICATION.....	iii
LIST OF ABBREVIATIONS AND SYMBOLS	iv
ACKNOWLEDGMENTS	ix
LIST OF FIGURES	xii
CHAPTER 1. INTRODUCTION	1
1.1 Background.....	3
CHAPTER 2. DERIVATION OF FORCES	7
2.1 Solar Radiation Pressure Model	7
2.2 Reflection Control Device Forces	12
2.3 Electromagnetic Wave Model	16
CHAPTER 3. DERIVATION OF TORQUES	33
3.1 Torque from Reflection Control Devices	34
3.2 Torque from Anomalous Reflections	39
CHAPTER 4. MANUFACTURE AND CHARACTERIZATION.....	44
4.1 Production of Graphene.....	45
4.1.1. Exfoliation/Cleavage	45
4.1.2. Epitaxial Growth/Chemical Vapor Deposition.....	49

4.1.3.	Thermal Decomposition On SiC:	49
4.1.4.	Chemically Derived Graphene	50
4.1.5.	Graphene Classification and Identification	51
4.1.6.	Discussion on Graphene	52
4.2	Characterization.....	64
CHAPTER 5. FUTURE RESEARCH PLANS		68
5.1	Designing and Modeling of ARM	69
5.2	Demonstration of Anomalous Reflection Force.....	70
5.3	Investigation of Integration on Solar Sail.....	72
CHAPTER 6. CONCLUSION.....		73
REFERENCES		76

LIST OF FIGURES

Figure 1.1 Photo of a solar sail (Source: NASA).....	1
Figure 1.2 (Top) Attitude control performance using reflection control device , (Bottom) IKAROS attitude control using reflection control device [1].....	3
Figure 1.3 Schematic of solar sail system interacting with oncoming TE polarized electromagnetic field. Angle of incidence is varied along the x-z plane. Background image was provided by NASA.	4
Figure 1.4 Schematics of an optical metamaterial planar structures (metasurface) that exhibits highly efficient anomalous reflection [9].....	6
Figure 2.1 Diagram of principal vectors from the solar radiation pressure model.	8
Figure 2.2 a) x component of force on the solar sail using tunable transmission RCDs. Line colors correspond to the frames on the legend above. b) z component of force on the solar sail using tunable transmission RCDs. Line colors correspond to the frames on the legend above.	14
Figure 2.3 a) x component of force on the solar sail using tunable absorption/emission RCDs. Line colors correspond to the frames on the legend above. b) z component of force on the solar sail using tunable absorption/emission RCDs. Line colors correspond to the frames on the legend above.	15
Figure 2.4 a) x component of force on the solar sail using tunable specular reflection RCDs. Line colors correspond to the frames on the legend above. b) z component of force on the solar sail using tunable specular reflection RCDs. Line colors correspond to the frames on the legend above.	16
Figure 2.5 (a) is a far field projection of the reflected electromagnetic wave with $\theta_r = 45^\circ$. Here θ_i is equal to 0° (i.e. normal to metasurface) and the polarization of electric field is in the \hat{y} direction. $\frac{\lambda}{a}$ and $\frac{2\pi}{\zeta}$ are the lattice constants for one unit-cell of the resonator arrays in \hat{y} and in \hat{x} directions, respectively. (b) is a plot of different angles of reflections that arise from using generalized Snell's law for anomalously reflected light. At $\zeta = 0$, the angle of reflection is the same as specularly reflected light. In the plot $\theta_{r,spec}$ refers to the specularly reflected wave, which is opposite sign to the incidence angle $\theta_{r,anom}$ refers to the angles of reflection of the anomalously reflected waves.	22
Figure 2.6 (a) is a plot of the anomalous reflection force (dashed green), specular reflection	

force (dashed red), incident electromagnetic force (solid black), and net force (bold green) for the lateral components of the solar sail. (b) is the same, but for the normal components. Both plots have the parameter $\zeta = 0.71k_0$. (c) is the ratio of the net forces from solely the specular case (bold red) and from the anomalous cases of varying phase gradient (the rest of the bold colors). All plots have the parameter $\eta_{anom} = 0.75$ 24

Figure 2.7 (a) is a plot of the anomalous reflection force (dashed), and net force (bold green) for the lateral components of the solar sail at different phase gradients. (b) is the same, but for the normal components. (c) is the optimal angle that produces the largest magnitude net force for both lateral (black) and normal (red) cases as a function of the phase gradient. All plots have the parameter, $\eta_{anom} = 0.75$ 27

Figure 2.8 (a) is a plot of the anomalous reflection force (dashed), and net force (bold green) for the lateral components of the solar sail at different values of anomalous conversion efficiency. (b) is the same, but for the normal components. (c) is the optimal angle that produces the largest magnitude net force for both lateral (black) and normal (red) cases as a function of the anomalous conversion efficiency. All plots have the parameter $\zeta = 0.71k_0$ 29

Figure 2.9 Plots of the net normal and lateral forces from anomalously reflecting metasurfaces for varying phase gradients, ζ . Both plots exhibit a scenerio where the metasurface anomalous conversion efficiency, η_{anom} , is 100%..... 31

Figure 3.1 x(pitch), y (yaw) and z (roll) components of torque on the solar sail using tunable transmission RCDs..... 37

Figure 3.2 x(pitch), y (yaw) and z (roll) components of torque on the solar sail using tunable absorption/emission RCDs..... 38

Figure 3.3 x(pitch), y (yaw) and z (roll) components of torque on the solar sail using tunable specular reflection..... 39

Figure 3.4 Torque along the pitch and yaw axes respectively. Both cases exhibit 100% anomalous efficiency ($\eta_{anom} = 1$)..... 43

Figure 4.1 Schematic diagram of the various stages of liquid phase exfoliation via sonication [26]..... 46

Figure 4.2 Images taken during the development process of the graphene ink. Large conglomerates of graphite chunks would accumulate in the petri dish after sonication(bottom left), The image on the bottom right is of the observed samples right after centrifugation. The sediment on the bottom of the tube contains larger chunks of graphene/graphite and is left behind after removing the supernatant. 55

Figure 4.3 shows the Raman Spectra of a sample of graphene ink solution. The expected G-Band peak of pure graphene is a wavenumber of $1580-1590\text{ cm}^{-1}$ 57

Figure 4.4 Schematic of the envisioned microfluidization process, based on [27].	59
Figure 4.5 Schematics of different setups for optical absorption modification in graphene-based devices. [40][43][44].	61
Figure 4.6 (a) Finite element modeling of the optical reflection and transmission of a single layer graphene near 5 μm that I realized using COMSOL Multiphysics. (b) Magnitude of the electric field of the electromagnetic wave as it propagates through the graphene	62
Figure 4.7 Examples of two deimsneional materials. The structures of these matherials allows for them to be easily stacked [45].	63
Figure 4.8 Illustration depicting the various scattering phenomena which can occur during the scattering of incident radiation. In Raman spectroscopy, the measured scattering are from the Stokes and Anti-Stokes Raman scattering [31].	64
Figure 5.1 Illustration of metasurfaces on a solar sail, resulting in in-plane tangential forces as a result of anomalous reflection of light.	72

CHAPTER 1. INTRODUCTION

The topic of this graduate research is the design, modeling, fabrication and characterization of metamaterials. Metamaterials are engineered sub-wavelength structures that are capable of intimate interaction with electromagnetic waves (e.g. light) to manipulate their propagation in space. The objective of this thesis is to design and demonstrate a type of metamaterial called Anomalously Reflecting Metasurfaces (ARM). This would address a current challenge of current solar sail propulsion technology: the inability to control roll, i.e. rotation around the axis normal to the sail (called roll-axis), without resorting to the use of propellant gas, that requires additional weight, power and complexity. Roll control is a critical element to balance the solar sail and attain the desired attitude.



Figure 1.1 Photo of a solar sail (Source: NASA).

The successful implementation of the proposed ARM with solar sail technology to achieve roll would drastically increase the attitude control capabilities of current solar sails and ultimately allow solar sails to become lighter, less complex and sustainable for long-term space

missions. As such, the proposed research can directly support current solar sail missions, such as the upcoming Near-Earth Asteroid (NEA) Scout mission being implemented by the National Aeronautic and Space Administration (NASA) at Marshall Space Flight Center (MSFC) and other future missions.

This graduate research work involves the design and modeling of metamaterial structures using multiphysics finite element analysis, studying the theory and fabrication techniques for metamaterial devices and developing theoretical derivations of metasurfaces on solar sails. These structures will be designed to be able to interact with visible and infrared photons, which are predominant in deep space. We are developing the means to dynamically change the torque on a solar sail in the desired directions by investigating the unique properties of anomalously reflecting metasurfaces. Our research will eventually allow us to fabricate proof-of-principle devices and measure their optical characteristics in support of the design and modeling work. We have made significant advancements in the theoretical derivations for metasurfaces on solar sails, began exploring different fabrication techniques that can be applied to developing ultra-thin metasurfaces, and developed computational models to characterize the force and torque of impinging photon radiation on a solar sail.

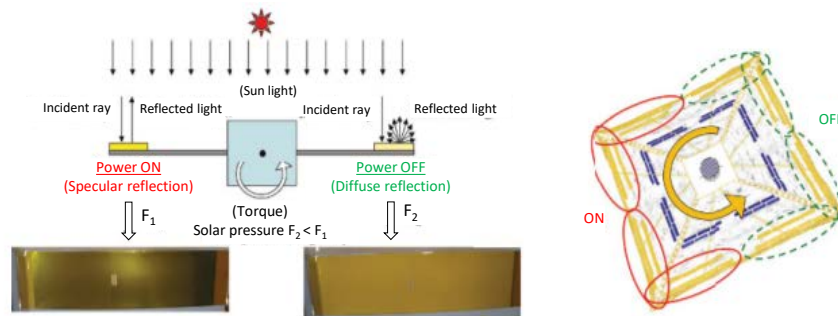
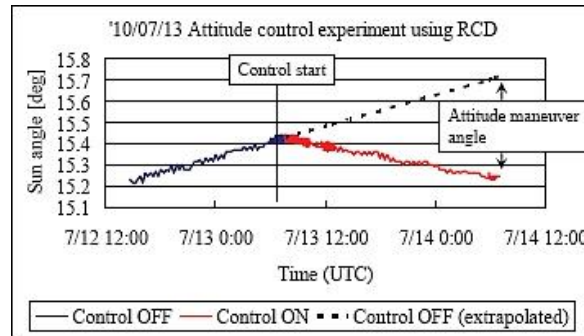


Figure 1.2 (Top) Attitude control performance using reflection control device, (Bottom) IKAROS attitude control using reflection control device [1].

In future years, it is anticipated that we will continue to work on metasurface integration with solar sails. In addition to optimizing the torque on the solar sail, we will explore different methods to dynamically alter the response of the solar sail forces. This may be due to either an induced electric dipole upon the metamaterial surface via a bias voltage, or a liquid crystal coating to alter the opacity of the surface medium preceding to the metasurface. We will work to design a metasurface that exhibits high anomalous reflection conversion efficiency.

1.1 Background

A pioneering example that paved the way for future development of solar sail research was the Interplanetary Kite-craft Accelerated by Radiation Of the Sun (IKAROS), made by the Japanese Aerospace Exploration Agency (JAXA). Launched in 2010, IKAROS was the first

demonstration of a spacecraft controlled via solar sails. The sail of IKAROS was made of ultra-thin polyimide resin with aluminum vapor deposited onto the front side of the membrane. Reflectivity control devices (RCDs) were utilized to change the angle of the sail with respect to the sun. This was done by electrically altering the reflectivity of liquid crystals, which were placed by the edges of the sail. The liquid crystals could be switched from specular to diffuse, thereby changing the torque exerted on the sail by sunlight, including a little bit of roll. However, this was not sufficient and propellant based solutions were still used. Despite this, IKAROS succeeded in providing proof that solar sail propulsion was an effective means for interplanetary travel, and demonstrated the importance of effective attitude control methods concerning photon angle of incidence.

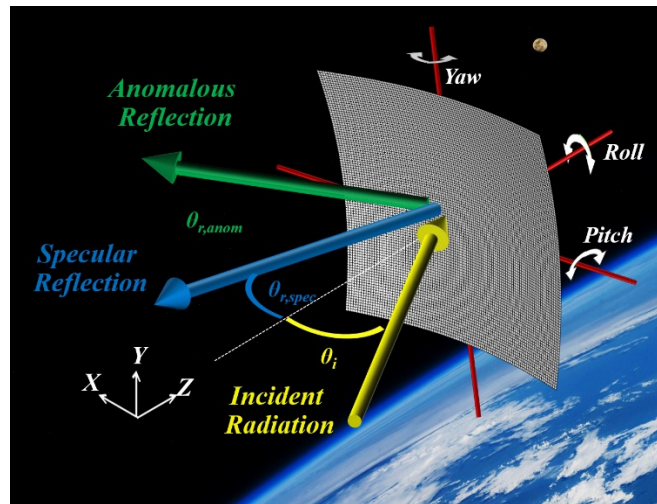


Figure 1.3 Schematic of solar sail system interacting with oncoming transverse electric polarized electromagnetic field. Angle of incidence is varied along the x-z plane. Background image was provided by NASA.

The success of IKAROS sparked further investigation into solar sail technology, leading to missions such as the Nano-Sail D mission, the LightSail projects, and the upcoming Near Earth Asteroid (NEA) Scout mission [2][3][4][5][6][7].

During the deployment of NASA's Near Earth Asteroid (NEA) Scout, solar sails will be utilized for propellant-free, sustainable propulsion. The solar sails will be deployed post-launch, and the NEA Scout's Attitude Control System (ACS) will be utilized to make corrections to the spacecraft's position and orientation as it travels. Two Primary methods of attitude control on the NEA Scout are the Active Mass Translator (AMT), and the cold gas thrusters, which are part of the Reaction Control System (RCS). The largest roll torque available to the NEA Scout is generated from the cold gas thrusters. The thrusters are angled in such a way that torque along any principal axis can be generated through firing of separate pairs of thrusters. The AMT shifts the center-of-mass to center-of-pressure (CM-CP) displacement. The torque on the sail is dependent upon the CM-CP displacement, so manipulating this displacement allows for some attitude control of the spacecraft.

Despite having attitude control systems already in place, problems can arise when the NEA Scout is in certain orientations with respect to strong light sources, such as when it is facing the Sun. In order to correct for undesirable fluctuations in incident photon radiation, controllable optical absorption in the solar sails would be ideal, as this would allow for adaptive attitude corrections. Additionally, another current technological limitation is the inability to achieve a high enough torque along the roll-axis, i.e. make the sail spin about its normal axis. A working, yet unsatisfactory, approach consists of using cold gas thrusters (requiring propellant) to make the sail roll, at the expense of weight, power and complexity. According to [8], in order for the NEA Scout solar sail to meet mission requirements, it would need to exhibit a torque along the roll axis on the order of $\sim 10 \text{ nN} \cdot \text{m}$ to be well within specifications. We will compare our results to this benchmark. The successful implementation of the proposed ARM with solar sail technology to achieve the desired roll torque would drastically increase the attitude control

capabilities of current solar sails and ultimately allow solar sails to become lighter, less complex, and sustainable for long-term space missions.

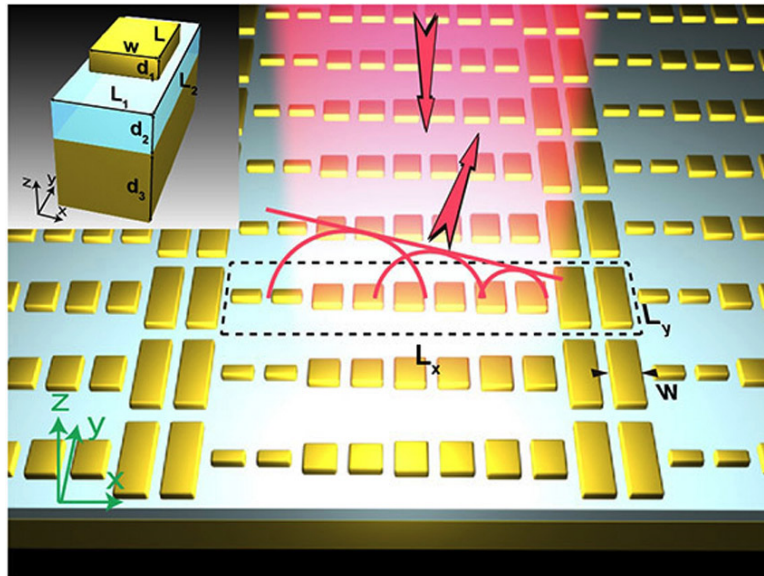


Figure 1.4 Schematics of an optical metamaterial planar structures (metasurface) that exhibits highly efficient anomalous reflection [9].

CHAPTER 2. DERIVATION OF FORCES

Before the force contributions from reflection control devices or anomalously reflecting metasurfaces are derived, we must first obtain a general force equation. In this chapter, I will cover the different approaches to deriving the forces on a solar sail.

2.1 Solar Radiation Pressure Model

The most commonly utilized force derivation for solar sails is called the solar radiation pressure model [10][11]. The total force is broken into three force components: transmission (\mathbf{F}_τ), absorption/emission (\mathbf{F}_γ), and reflection (\mathbf{F}_ρ).

$$\tau_r = \text{transmission coefficient}$$

$$\gamma = \text{absorption/emission coefficient}$$

$$\rho = \text{reflection coefficient}$$

$$\tau_r + \gamma + \rho = 1 \quad (2.1)$$

$$\mathbf{F}_{tot} = \tau_r \mathbf{F}_\tau + \gamma \mathbf{F}_\gamma + \rho \mathbf{F}_\rho \quad (2.2)$$

The main vectors to consider are the normal unit vector, \mathbf{n} , which is perpendicular to the solar sail surface, and the unit vector for photon direction of incidence, \mathbf{u} , which is parallel to the incoming radiation. A diagram of the system is shown in Figure 2.1.

The transmission component is typically taken to be zero because solar sail surfaces are opaque,

$$\tau_r \mathbf{F}_\tau = 0. \quad (2.3)$$

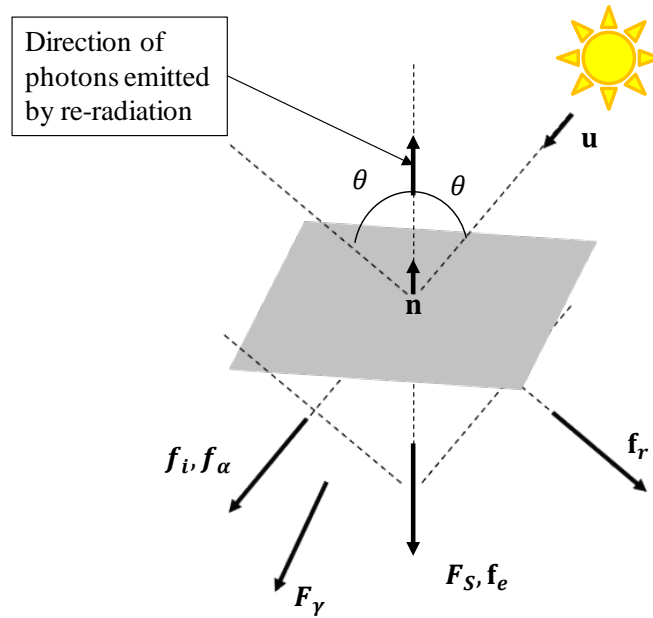


Figure 2.1 Diagram of principal vectors from the solar radiation pressure model.

To find the force contribution from the light absorbed by the solar sail surface, we need to consider both the absorption and emission of photons. The absorption/emission component is broken up into two separate contributions: a part directly related to the absorption of a photon, f_α , and a part pertaining to the emission by re-radiation, f_e . For the case of absorption,

$$\mathbf{f}_\alpha = \frac{dp}{dt} \mathbf{u} = \frac{1}{c} \frac{dE}{dt} \mathbf{u} = \frac{1}{c} W \cos(\theta) dS \mathbf{u} \quad (2.4)$$

Absorbed photons generate a force in the direction of the incident beam because of photon momentum transfer.

$$(\epsilon_f + \epsilon_b) \sigma T_{eq}^4 = W \cos(\theta) \quad (2.5)$$

$$T_{eq} = \sqrt[4]{\frac{\gamma W \cos(\theta)}{\sigma(\epsilon_f + \epsilon_b)}} \quad (2.6)$$

For the emission component,

$$\begin{aligned} \mathbf{f}_e &= \frac{\sigma T_{eq}^4}{c} (\epsilon_f B_f + \epsilon_b B_b) dS \mathbf{n} = \frac{\sigma^4 \sqrt{\frac{\gamma W \cos(\theta)}{\sigma(\epsilon_f + \epsilon_b)}}}{c} (\epsilon_f B_f + \epsilon_b B_b) dS \mathbf{n} \\ &= \frac{W \cos(\theta)}{c} \frac{(\epsilon_f B_f + \epsilon_b B_b)}{(\epsilon_f + \epsilon_b)} dS \mathbf{n} \end{aligned} \quad (2.7)$$

Photons are emitted in a direction normal to the solar sail surface, so the force will be in the opposite direction, also parallel to the normal vector.

Combining the absorption and emission terms, the total force contribution from the absorption of incident light on the solar sail comes out to be,

$$\begin{aligned} \mathbf{F}_\gamma &= \frac{1}{c} W \cos(\theta) dS \mathbf{u} + \frac{W \cos(\theta)}{c} \frac{(\epsilon_f B_f + \epsilon_b B_b)}{(\epsilon_f + \epsilon_b)} dS \mathbf{n} \\ &= \frac{W \cos(\theta) dS}{c} \left(\mathbf{u} + \frac{(\epsilon_f B_f + \epsilon_b B_b)}{(\epsilon_f + \epsilon_b)} \mathbf{n} \right) \end{aligned} \quad (2.8)$$

The final component of force to consider is the force due to the reflection of light from the solar sail. This force must also be further divided into two different components, namely from the specular reflections, ρ_s , and the diffuse reflections, ρ_d .

$$\rho \mathbf{F}_\rho = s \mathbf{F}_s + d \mathbf{F}_d, \quad (2.9)$$

where the coefficients s and d , combine to equal the total reflectivity coefficient, ρ .

$$\rho = s + d \quad (2.10)$$

$$\begin{aligned} \mathbf{F}_s &= \mathbf{f}_i + \mathbf{f}_r = \frac{1}{c} W \cos(\theta) dS \mathbf{u} - \frac{1}{c} W \cos(\theta) dS \mathbf{u}_r \\ &= -\frac{2W}{c} \cos^2(\theta) dS \mathbf{n} \end{aligned} \quad (2.11)$$

Specular reflections angles are equal in magnitude to the incidence angle and will have both equal and opposite tangential components. This results in a purely normal component of the specular reflection force.

Diffuse reflections can be derived in a similar manner of adding up the force from the incident solar radiation and its reflections.

$$\mathbf{F}_d = \mathbf{f}_i + \mathbf{f}_r \quad (2.12)$$

In the case of diffuse reflection, however, there is a few more angles to consider. The incident radiation force can be found to be,

$$\mathbf{f}_i = \frac{1}{c} W \cos(\theta) dS \mathbf{u}. \quad (2.13)$$

The reflection angle is found by considering the reflections due to Lambert diffusion. The radiant intensity, I_Ω , for a Lambert diffuser has a dependent relationship with the observation angle, Θ , which varies with the cosine of Θ . Apparent brightness is related to the radiant intensity divided by the projected area of the surface being considered. Since the projected area of the surface also depends on the observation angle by $\cos(\Theta)$, the expression for apparent brightness will have both terms of $\cos(\Theta)$ cancel out. The apparent brightness will not change with the observation angle. Next, to find the reflection angle, we will need to consider the sum of all reflected light over the span of multiple different angles. $d\Omega$ is a differential area of a semi-circle disk, and takes into account a clock angle/polar angle, ϕ .

$$d\Omega = d\theta d\phi \sin(\theta) R^2 \quad (2.14)$$

Next, we define the radiant intensity to be,

$$I_\Omega = I_{Max} \cos(\theta) \quad (2.15)$$

One we find the radiant intensity, we can find the radiant flux by integrating over the entire area $d\Omega$.

$$\begin{aligned}
total\ flux &= W \cos(\theta) dS = \int I_{\Omega} d\Omega = \int I_{Max} \cos(\theta) d\Omega \\
&= \int_0^{\frac{\pi}{2}} \int_0^{2\pi} I_{Max} \cos(\theta) \sin(\theta) R^2 d\phi d\theta = 2\pi R^2 I_{Max} \int_0^{\frac{\pi}{2}} \cos(\theta) \sin(\theta) d\theta = \pi R^2 I_{Max} \quad (2.16)
\end{aligned}$$

$$I_{Max} = \frac{W \cos(\theta) dS}{\pi R^2} \quad (2.17)$$

$$\begin{aligned}
W_{d\Omega} &= I_{\Omega} d\Omega = \frac{W \cos(\theta) dS}{\pi R^2} \cos(\theta) d\theta d\phi \sin(\theta) R^2 \\
&= \frac{W \cos(\theta) dS}{\pi} \cos(\theta) \sin(\theta) d\theta d\phi \quad (2.18)
\end{aligned}$$

Finally, the diffuse reflection force for a finite element of the semi-circle disk can be found to be,

$$\mathbf{f}_{d\Omega} = \frac{W_{d\Omega}}{c} = \frac{W \cos(\theta) dS}{\pi c} \cos(\theta) \sin(\theta) d\theta d\phi, \quad (2.19)$$

Then finally integrated over the whole surface to find the total reflection force from diffuse reflections.

$$\begin{aligned}
\mathbf{f}_r &= \int \int \cos(\theta) \mathbf{f}_{d\Omega} \cdot (-\mathbf{n}) = \int_0^{\frac{\pi}{2}} \int_0^{2\pi} \frac{W \cos(\theta) dS}{\pi c} \cos^2(\theta) \sin(\theta) d\theta d\phi \cdot (-\mathbf{n}) \\
&= \frac{2}{3} \frac{W \cos(\theta) dS}{c} \cdot (-\mathbf{n}) \quad (2.20)
\end{aligned}$$

On a Lambertian surface, diffuse reflections are reflected at all angles centered on the point of photon interaction- so they cancel each other and there is also no tangential force. However, for a non-perfect Lambertian, diffusely reflecting surface, there is a tangential component

$$\mathbf{F}_d = \frac{W \cos(\theta)}{c} \cdot \left(\mathbf{u} - \frac{2}{3} \mathbf{n} \right) dS \quad (2.21)$$

$$\mathbf{F}_d = \frac{W \cos(\theta)}{c} \cdot (\mathbf{u} - B_f \mathbf{n}) dS \quad (2.22)$$

Adding all of the previously combined components, we are able to obtain an analytical expression for the total force on a solar sail system.

$$\mathbf{F}_{tot} = \frac{W}{c} \left(\gamma \cos(\theta) \left(\mathbf{u} + \frac{(\epsilon_f B_f + \epsilon_b B_b)}{(\epsilon_f + \epsilon_b)} \mathbf{n} \right) - 2s \cos^2(\theta) \mathbf{n} + d \cos(\theta) (\mathbf{u} - B_f \mathbf{n}) \right) dS \quad (2.23)$$

$$\mathbf{F}_{tot} = -P(\mathbf{u} \cdot \mathbf{n}) \left(\gamma \mathbf{u} + \gamma \frac{(\epsilon_f B_f + \epsilon_b B_b)}{(\epsilon_f + \epsilon_b)} \mathbf{n} + 2s(\mathbf{u} \cdot \mathbf{n}) \mathbf{n} + d(\mathbf{u} - B_f \mathbf{n}) \right) dS \quad (2.24)$$

$$\tau_r + \gamma + s + d = 1 \quad (2.25)$$

It will be useful when considering the torque on the solar sail along the pitch, yaw and roll axes, to consider the normal and tangential forces separately.

$$\mathbf{F}_{tot,t} = -\gamma P(\mathbf{u} \cdot \mathbf{n})(\mathbf{u} \cdot \mathbf{t}) dS \cdot \mathbf{t} \quad (2.26)$$

$$\mathbf{F}_{tot,n} = -P(\mathbf{u} \cdot \mathbf{n}) \left((\gamma + d + 2s) \mathbf{u} \cdot \mathbf{n} + \gamma \frac{(\epsilon_b B_b - \epsilon_f B_f)}{(\epsilon_f + \epsilon_b)} - d B_f \right) dS \cdot \mathbf{n} \quad (2.27)$$

For purely specular reflection, $\rho_s = 1$ and

$$\mathbf{F}_{tot} = -2P(\mathbf{u} \cdot \mathbf{n})^2 dS \cdot \mathbf{n} \quad (2.28)$$

$$\mathbf{F}_{tot} = -PA(\mathbf{u} \cdot \mathbf{n}) \left(\gamma \mathbf{u} + \gamma \frac{\epsilon_b B_b - \epsilon_f B_f}{\epsilon_f + \epsilon_b} \mathbf{n} + 2s(\mathbf{u} \cdot \mathbf{n}) + d(\mathbf{u} - B_f \mathbf{n}) \right) \quad (2.29)$$

$$\mathbf{F}_{tot,t} = -\gamma PA(\mathbf{u} \cdot \mathbf{n})(\mathbf{u} \cdot \mathbf{t}) \cdot \mathbf{t} \quad (2.30)$$

2.2 Reflection Control Device Forces

Now that we have the general equations for the force on a solar sail according to the solar radiation pressure model, we can alter the parameters to be consistent with technology that has been demonstrated. The reflection control devices on IKAROS were able to switch between having reflections that were specular, to reflections that were diffuse. To emulate the RCDs, we

can switch the parameter s to change from zero to one. This would mean that the reflections on the solar sail would be changed from perfectly diffuse, to perfectly specular reflections.

Over the course of the rest of this thesis, I will be referring to five main geometric configurations of devices on the surface of the solar sail. The devices will be spread on the surface of the solar sail so that one or more of the optical properties of a section of the sail is changed. The net force will then be different from the case where the sail was uniform across the whole surface.

The cases I have considered will be depicted with a matrix of 1's and 0's, with the 0's indicating the "OFF" state of the devices, and the 1's indicating the "ON" state. The five cases are as follows:

$$\begin{array}{cccc} \text{Case 1:} \begin{pmatrix} 1 & 1 \\ 1 & 1 \end{pmatrix} & \text{Case 2:} \begin{pmatrix} 1 & 1 \\ 0 & 0 \end{pmatrix} & \text{Case 3:} \begin{pmatrix} 1 & 0 \\ 1 & 0 \end{pmatrix} & \text{Case 4:} \begin{pmatrix} 1 & 0 \\ 0 & 1 \end{pmatrix} \\ & & & \text{Case 5:} \begin{pmatrix} 1 & 1 & 1 & 1 \\ 1 & 1 & 1 & 0 \\ 1 & 1 & 0 & 0 \\ 1 & 0 & 0 & 0 \end{pmatrix}. \end{array}$$

Figure 2.2, 2.3, and 2.4 show the plots of the normal and tangential force components on the solar sail from varying different optical properties of the solar sail.

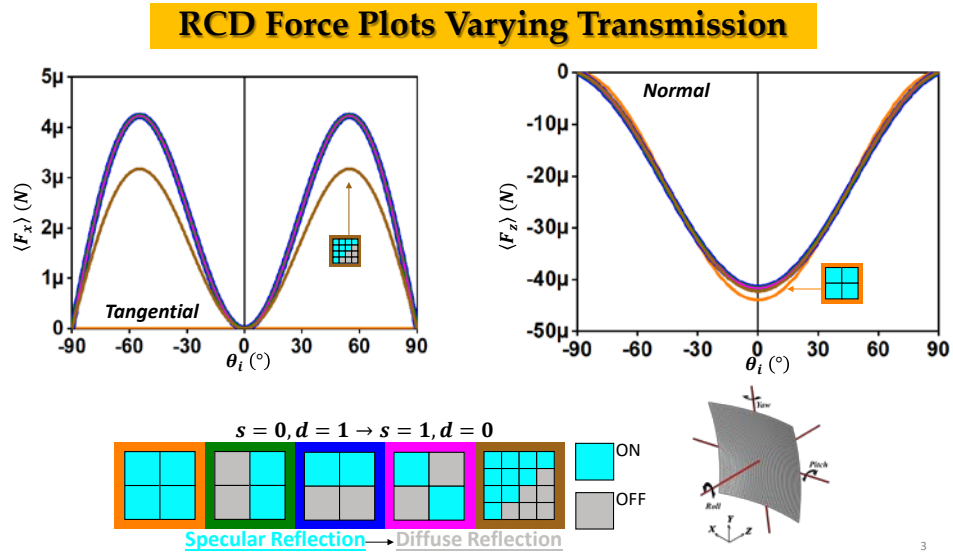


Figure 2.2 a) x component of force on the solar sail using tunable transmission RCDs. Line colors correspond to the frames on the legend above. b) z component of force on the solar sail using tunable transmission RCDs. Line colors correspond to the frames on the legend above.

RCD Force Plots Varying Absorption/Emission

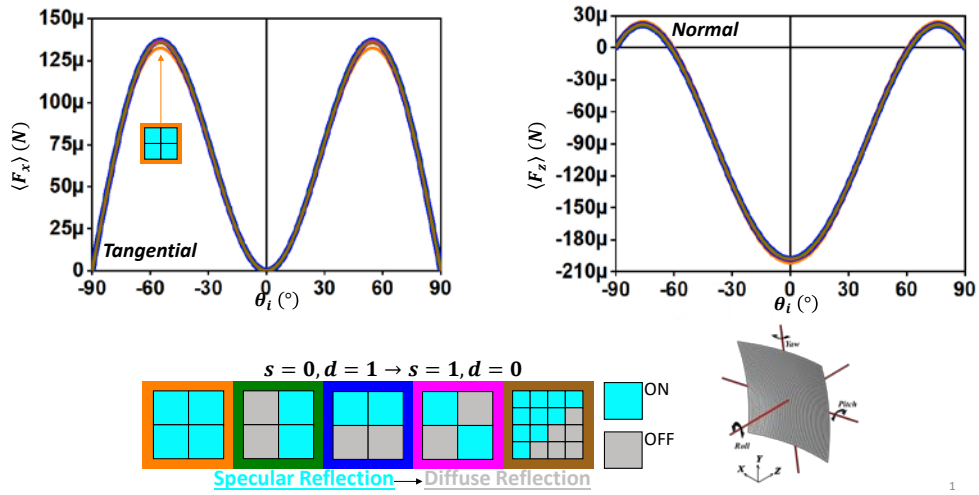


Figure 2.3 a) x component of force on the solar sail using tunable absorption/emission RCDs. Line colors correspond to the frames on the legend above. b) z component of force on the solar sail using tunable absorption/emission RCDs. Line colors correspond to the frames on the legend above.

RCD Force Plots Varying Specular Reflectivity

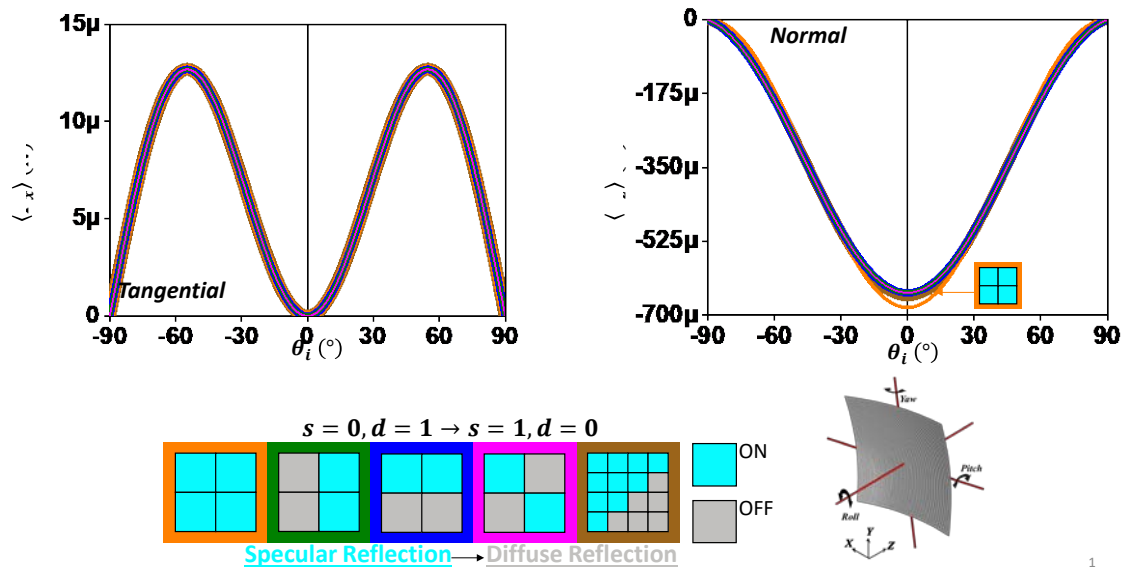


Figure 2.4 a) x component of force on the solar sail using tunable specular reflection RCDs. Line colors correspond to the frames on the legend above. b) z component of force on the solar sail using tunable specular reflection RCDs. Line colors correspond to the frames on the legend above.

The main purpose of these plots is to serve as a point of comparison between the next set of derivations that we cover, which are due to anomalously reflecting metasurfaces. Figure 2.4, in particular, will be a good reference plot to represent real life technology that has been demonstrated, namely IKAROS. As can be seen from the plot, very small lateral forces are produced compared to the much large magnitude normal forces.

2.3 Electromagnetic Wave Model

The first task is to define the plane wave incident on the solar sail. The plane wave is simplified to only be in the x-z plane, and the surface is isotropic. $\epsilon = \epsilon_0 ; \mu = \mu_0 ; \eta = \eta_0 =$

$$\sqrt{\frac{\mu_0}{\epsilon_0}}$$

Using a p-polarized plane waves as the source of incident radiation, the total vector fields are:

$$E_{i,x} = E_0 e^{-i k_0 (\sin(\theta)x + \cos(\theta)z)} \cos(\theta) \quad (2.31)$$

$$E_{i,y} = 0 \quad (2.32)$$

$$E_{i,z} = -E_0 e^{-i k_0 (\sin(\theta)x + \cos(\theta)z)} \sin(\theta) \quad (2.33)$$

$$H_{i,x} = 0 \quad (2.34)$$

$$H_{i,y} = \frac{E_0}{\eta_0} e^{-i k_0 (\sin(\theta)x + \cos(\theta)z)} \quad (2.35)$$

$$H_{i,z} = 0 \quad (2.36)$$

$$\mathbf{E}_i = E_{i,x} \hat{x} + E_{i,y} \hat{y} + E_{i,z} \hat{z} \quad (2.37)$$

$$\mathbf{H}_i = H_{i,x} \hat{x} + H_{i,y} \hat{y} + H_{i,z} \hat{z} \quad (2.38)$$

$$\mathbf{D}_i = \epsilon_0 \mathbf{E}_i \quad (2.39)$$

$$\mathbf{B}_i = \mu_0 \mathbf{H}_i \quad (2.40)$$

Solar sails are a viable form of transportation because photons have momentum. The conservation of momentum law for electromagnetic waves can be related to solids through the following equation:

$$\mathbf{f} + \epsilon\mu \frac{\partial \mathbf{S}}{\partial t} = \nabla \cdot \vec{\mathbf{T}} \quad (2.41)$$

$\vec{\mathbf{T}}$ is the Maxwell Stress Tensor that represents the interaction between the momentum from an electromagnetic wave, and mechanical momentum. We can make the simplification that the object is not moving, so the field around the object is not changing with time, so $\frac{\partial \mathbf{S}}{\partial t} = 0$. The \mathbf{f} is the force volume density, and integrating over a volume would allow the total force to be calculated. Using Gauss integration law, we can instead relate the time-averaged force to the net flux from the Maxwell Stress Tensor through the solar sail surface, S .

$$\vec{T} = \mathbf{D} \otimes \mathbf{E} + \mathbf{B} \otimes \mathbf{H} - \frac{1}{2} \bar{I} (\mathbf{D} \cdot \mathbf{E} + \mathbf{B} \cdot \mathbf{H}) \quad (2.42)$$

$$\langle \mathbf{F} \rangle = \int_V \nabla \cdot \langle \vec{T} \rangle dV = \oint_S \langle \vec{T} \rangle \cdot \hat{\mathbf{n}} dS \quad (2.43)$$

$$\vec{T} = \mathbf{D}_i \otimes \mathbf{E}_i + \mathbf{B}_i \otimes \mathbf{H}_i - \frac{1}{2} \begin{bmatrix} 1 & 0 & 0 \\ 0 & 1 & 0 \\ 0 & 0 & 1 \end{bmatrix} (\mathbf{D}_i \cdot \mathbf{E}_i + \mathbf{B}_i \cdot \mathbf{H}_i) \quad (2.44)$$

$$\begin{aligned} \langle \vec{T} \rangle &= \frac{1}{2} \text{Re}[\vec{T}] = \frac{1}{2} \cos(\theta) \sin(\theta) \epsilon_0 E_0^2 \hat{\mathbf{x}} \\ &+ \frac{1}{2} e^{2i(z \cos(\theta) + x \sin(\theta))k_0} \left(-e^{-2i(z \cos(\theta) + x \sin(\theta))k_0} \sin(\theta)^2 \epsilon_0 E_0^2 \right. \\ &+ \frac{1}{2} \left(e^{-2i(z \cos(\theta) + x \sin(\theta))k_0} \epsilon_0 E_0^2 + e^{-2i(z \cos(\theta) + x \sin(\theta))k_0} \cos(\theta)^2 \epsilon_0 E_0^2 \right. \\ &\left. \left. + e^{-2i(z \cos(\theta) + x \sin(\theta))k_0} \sin(\theta)^2 \epsilon_0 E_0^2 \right) \right) \hat{\mathbf{z}} \end{aligned} \quad (2.45)$$

The normal vector, $\hat{\mathbf{n}} = -\hat{\mathbf{z}}$ for the incident wave

$$\begin{aligned} \frac{1}{2} \text{Re}[\vec{T}] \cdot (\hat{\mathbf{n}}) &= \frac{1}{2} \text{Re}[\overline{T_{em}}] \cdot (-\hat{\mathbf{z}}) = \\ \frac{1}{2} E_0^2 \epsilon_0 \sin(\theta) \cos(\theta) \hat{\mathbf{x}} &+ \frac{1}{2} E_0^2 \epsilon_0 \cos^2(\theta) \hat{\mathbf{z}} \end{aligned} \quad (2.46)$$

The time-averaged force components can then be found by integrating over the surface of the solar sail:

$$\begin{aligned} \langle \mathbf{F}_{i,\parallel} \rangle &= \int_{y=0}^{y=L_y} \int_{x=0}^{x=L_x} \frac{1}{2} E_0^2 \epsilon_0 \sin(\theta) \cos(\theta) dx dy \hat{\mathbf{x}} = \\ \frac{1}{2} E_0^2 \epsilon_0 \sin(\theta) \cos(\theta) L_x L_y \hat{\mathbf{x}} & \end{aligned} \quad (2.47)$$

$$\begin{aligned}\langle \mathbf{F}_{i,\perp} \rangle &= \int_{y=0}^{y=L_y} \int_{x=0}^{x=L_x} \frac{1}{2} E_0^2 \epsilon_0 \cos^2(\theta) dx dy \hat{\mathbf{z}} = \\ &= \frac{1}{2} E_0^2 \epsilon_0 \cos^2(\theta) L_x L_y \hat{\mathbf{z}}\end{aligned}\quad (2.48)$$

In the same way that the incident wave creates a force, the reflected and transmitted waves also exert a force on the sail. Since Snell's Law of Reflection dictates that $\theta_i = -\theta_r$, the reflected wave will have an in-plane force in the opposite direction to the incident wave (because $\sin(-\theta) = -\sin(\theta)$) and an out-of-plane force in the same direction (because $\cos(-\theta) = \cos(\theta)$). For our purposes, it can be said that the transmitted force is effectively zero, as this is most often the case with current solar sail technology.

$$\langle \mathbf{F}_{i,\parallel} \rangle = -\langle \mathbf{F}_{r,\parallel} \rangle ; \langle \mathbf{F}_{i,\perp} \rangle = \langle \mathbf{F}_{r,\perp} \rangle \quad (2.49)$$

$$\langle \mathbf{F}_{t,\parallel} \rangle = 0 ; \langle \mathbf{F}_{t,\perp} \rangle = 0 \quad (2.50)$$

For the case involving the field configurations that give rise to a lateral force, the out-of-plane force will need to be added together. Since the plane wave is only in the x-z plane, there is only an x-component that is in-plane. The net lateral force will be from the different $\langle F_x \rangle$ terms.

$$\langle \mathbf{F}_{i,\parallel} \rangle = \frac{1}{2} E_0^2 \epsilon_0 L_x L_y \sin(\theta) \cos(\theta) \hat{\mathbf{x}} \quad (2.51)$$

$$\langle \mathbf{F}_{r,\parallel} \rangle = \frac{1}{2} E_0^2 \epsilon_0 L_x L_y \sin(-\theta) \cos(-\theta) \hat{\mathbf{x}} \quad (2.52)$$

$$\langle \mathbf{F}_{\parallel} \rangle = \langle \mathbf{F}_{i,\parallel} \rangle + \langle \mathbf{F}_{r,\parallel} \rangle = 0 \quad (2.53)$$

In the typical case where solar sails follow Snell's Law of Reflection ($|\theta_i| = |\theta_r|$), there is a negligible net lateral force.

For the normal force,

$$\langle \mathbf{F}_{i,\perp} \rangle = \frac{1}{2} E_0^2 \epsilon_0 \cos^2(\theta) L_x L_y \hat{\mathbf{z}} \quad (2.54)$$

$$\langle \mathbf{F}_{r,\perp} \rangle = \frac{1}{2} E_0^2 \epsilon_0 \cos^2(\theta) L_x L_y \hat{\mathbf{z}} \quad (2.55)$$

$$\langle \mathbf{F}_\perp \rangle = \langle \mathbf{F}_{i,\perp} \rangle + \langle \mathbf{F}_{r,\perp} \rangle = E_0^2 \epsilon_0 \cos^2(\theta) L_x L_y \hat{\mathbf{z}} \quad (2.56)$$

To our knowledge, anomalously reflecting metasurfaces have never before been considered for solar sail applications. In order to gain key insights that could be utilized when designing the metasurfaces, it was critical to develop analytical equations that can describe the tangential forces on a solar sail from anomalously reflected light. The forces from a plane wave on a solar sail can be found from using the Maxwell Stress Tensor in the law of conservation of momentum equation [12][13][14]. The incident wave, the reflected wave, and the transmitted wave, all have momentum and energy, so they will all generate a force on the solar sail [12]

[13]. In most cases, however, solar sails are made out of highly reflective materials that allow for no transmitted waves, so the transmitted term can be neglected.

As previously stated, the most commonly recognized version of Snell's law of reflection states that $\theta_i = \theta_r$. When this is the case, the net force from the incident and reflected waves will have only a normal component. The tangential component of the net force will be negligible because the tangential forces from the incident and reflected waves will be equal and opposite, canceling each other out. This is the primary reason why no torque can be generated along the roll axis of the sail. Without any net tangential force along the edges of the sail, then there can be no rotation.

For anomalous reflecting surfaces, $\theta_i \neq \theta_r$, so the forces do not cancel out. This means that there is a net tangential force on the sail.

Starting from the equation for generalized Snell's law of reflection, we will derive the forces from anomalously reflected waves. The expression for the generalized Snell's law of reflection is

$$\sin \theta_r - \sin \theta_i = \frac{1}{n_i k_0} \frac{\partial \Phi}{\partial x} \quad (2.57)$$

which includes a phase gradient, $\frac{\partial \Phi}{\partial x}$, that is introduced by the metasurface that interacts with the incident light[15][16][17][18][19][20].

One particular design that offers considerable promise to maximize the anomalous reflection of incident light is a gradient metasurface. The design consists of an array of symmetric rectangular metal patches with every other patch having a different size in order to induce the appropriate phase gradient for anomalous reflection. These metasurfaces can produce a constant phase gradient that is entirely dependent upon the geometric parameters of the structures.

In the case of the gradient metasurface, the phase gradient will be equal to a constant.

$$\frac{\partial \Phi}{\partial x} = \zeta \quad (2.58)$$

The dimensions of the phase gradient metasurface can be found by incorporating a modified diffraction equation into the generalized Snell's law equation, to obtain $\zeta = \frac{2\pi}{l_x}$, though the length of the supercell (the metamaterial gradient structure), is not important for our purposes. More generally, we can choose a phase gradient that will provide our desired reflection angle from normally incident light. For example, if we want normally incident light to be reflected at an angle of 90° , then we can use the phase gradient

$$\zeta = k_0(\sin 90^\circ - \sin 0^\circ) = k_0 \quad (2.59)$$

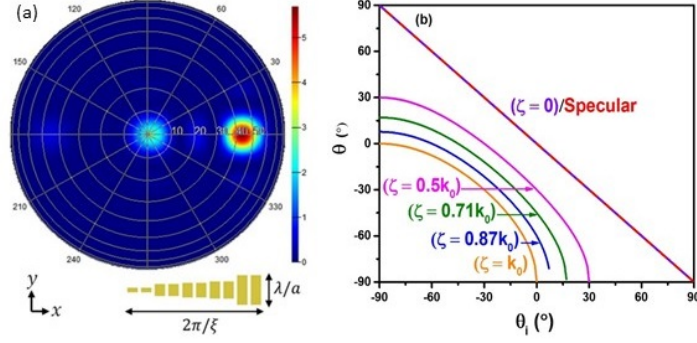


Figure 2.5 (a) is a far field projection of the reflected electromagnetic wave with $\theta_r = 45^\circ$. Here θ_i is equal to 0° (i.e. normal to metasurface) and the polarization of electric field is in the \hat{y} direction. $\frac{\lambda}{a}$ and $\frac{2\pi}{\zeta}$ are the lattice constants for one unit-cell of the resonator arrays in \hat{y} and in \hat{x} directions, respectively. (b) is a plot of different angles of reflections that arise from using generalized Snell's law for anomalously reflected light. At $\zeta = 0$, the angle of reflection is the same as specularly reflected light. In the plot $\theta_{r,spec}$ refers to the specularly reflected wave, which is opposite sign to the incidence angle $\theta_{r,anom}$ refers to the angles of reflection of the anomalously reflected waves.

Once we have chosen a phase gradient, we can then use the value of ζ in the generalized Snell's law expression to solve for the reflection angle

$$\theta_r = \sin^{-1} \left(\frac{1}{n_i k_0} \zeta + \sin \theta_i \right). \quad (2.60)$$

The plot in Figure 2.5b shows how the angle of anomalous reflection differs from the angle of regular reflection. From the plot, it should be mentioned that there is a point where the angle of anomalous reflection becomes imaginary. When $\sin \theta_i > 1 - \frac{1}{n_i k_0} \zeta$, the value inside of the Arcsine becomes greater than unity, which causes the expression to become complex and the propagating waves are converted into surface waves in the metasurface [21]. The new Maxwell stress tensor is

$$\vec{T}_r = \frac{E_0^2 \alpha}{2k_0^2 \eta_0^2} \begin{pmatrix} -(k_0^2 \epsilon_0 \eta_0^2 + \beta \mu_0) & 0 & \delta \\ 0 & k_0^2 (\epsilon_0 \eta_0^2 - \mu_0) & 0 \\ \delta & 0 & -(k_0^2 \epsilon_0 \eta_0^2 - \beta \mu_0) \end{pmatrix} \quad (2.61)$$

where,

$$\alpha = e^{\left(2i \left(x\zeta + x \sin(\theta) k_0 - z \sqrt{1 - \left(\frac{\zeta}{k_0} + \sin(\theta) \right)^2} k_0 \right) \right)} \quad (2.62)$$

$$\beta = (2\zeta^2 + 4\sin(\theta)k_0\zeta - \cos(2\theta)k_0^2) \quad (2.63)$$

$$\delta = 2k_0\mu_0(\zeta + \sin(\theta)k_0) \sqrt{1 - \left(\frac{\zeta}{k_0} + \sin(\theta) \right)^2} \quad (2.64)$$

The plane wave force was found to be

$$\langle \mathbf{F}_{r,\perp} \rangle = \frac{L_x L_y E_0^2}{4\eta_0^2 k_0^2} (\mu_0 (-2\zeta^2 - 4\zeta k_0 \sin(\theta) + k_0^2 \cos(2\theta)) + \eta_0^2 k_0^2 \epsilon_0) \hat{\mathbf{z}} \quad (2.65)$$

$$\langle \mathbf{F}_{r,\parallel} \rangle = -\frac{\mu_0 L_x L_y E_0^2}{2\eta_0^2 k_0} (\zeta + k_0 \sin(\theta)) \sqrt{1 - \left(\sin(\theta) + \frac{\zeta}{k_0} \right)^2} \hat{\mathbf{x}} \quad (2.66)$$

Inserting the derived expression for the anomalous angle of reflection into the tangential force equation for θ_r , and then adding the result to the incident tangential force, we obtain,

$$\begin{aligned} \langle \mathbf{F}_x \rangle &= \langle \mathbf{F}_x \rangle_i + \langle \mathbf{F}_x \rangle_r = \\ & \frac{\mu_0 L_x L_y E_0^2}{2\eta_0^2} \left(\sin(\theta) \cos(\theta) - \frac{(\zeta + k_0 \sin(\theta))}{k_0} \sqrt{1 - \left(\sin(\theta) + \frac{\zeta}{k_0} \right)^2} \right) \end{aligned} \quad (2.67)$$

One thing that is important to note is that the anomalously reflected light should have the same polarization as the incident fields when using the gradient metamaterial structures [15].

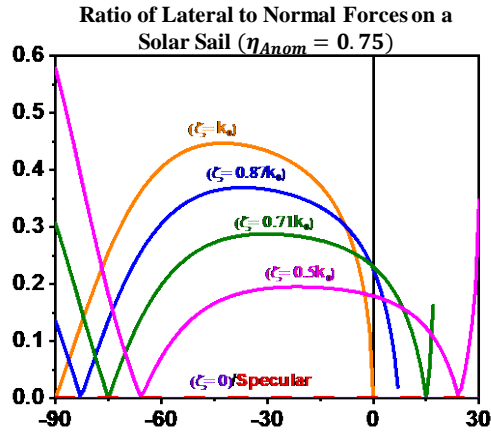
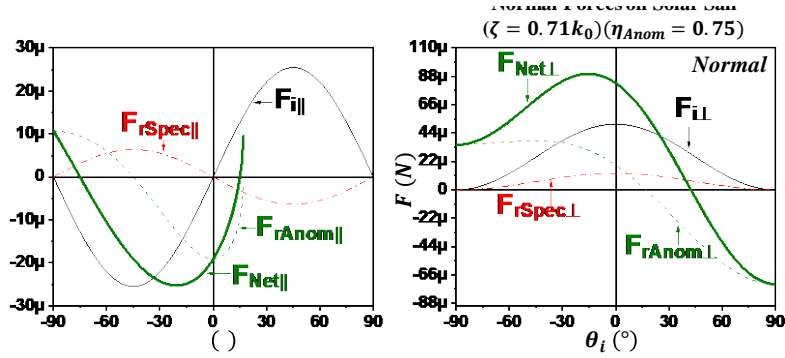


Figure 2.6 (a) is a plot of the anomalous reflection force (dashed green), specular reflection force (dashed red), incident electromagnetic force (solid black), and net force (bold green) for the lateral components of the solar sail. (b) is the same, but for the normal components. Both plots have the parameter $\zeta = 0.71k_0$. (c) is the ratio of the net forces from solely the specular case (bold red) and from the anomalous cases of varying phase gradient (the rest of the bold colors). All plots have the parameter $\eta_{anom} = 0.75$.

Figure 2.6a and b display the force contributions from anomalous reflections and regular reflections in the normal and lateral cases, respectively. In order to make our results consistent with reality, we included an efficiency scaling factor.

The specular and anomalous reflection components are scaled by an anomalous conversion efficiency factor, η_{anom} . It is observed for anomalously reflecting metasurfaces, a

certain amount of the reflected light will always be specularly reflected. We chose to use a phase gradient of $0.71k_0$, and an anomalous conversion efficiency of 0.75. These values are consistent with [18]. Therefore, the net force on the solar sail can be evaluated by adding the force from the incident wave to the forces from the anomalous and specular reflections, $\langle F_x \rangle_i + (1 - \eta_{anom})\langle F_x \rangle_{r,spec} + (\eta_{anom})\langle F_x \rangle_{r,anom} = \langle F_x \rangle_{Net}$. The bold lines displayed in Figure 2.6a and 2.6b are the net forces, with the green lines corresponding to the parameters $\zeta = 0.71k_0$ and $\eta_{anom} = 0.75$. The plot in Figure 2.6c shows the proportion of net lateral force to the net normal force with varying phase gradient ζ . All of the colored lines show the ratio of net forces for the cases that include anomalous reflections, $\frac{\langle F_x \rangle_{Net}}{\langle F_z \rangle_{Net}}$, except for the red line, which represents the purely specular case, $\frac{\langle F_x \rangle_i + \langle F_x \rangle_{r,spec}}{\langle F_z \rangle_i + \langle F_z \rangle_{r,spec}}$, which becomes zero.

In the case of the metasurface we have chosen to focus on (green) in Figure 2.6c, the lateral-to-normal force ratio is locally maximized at $\theta = -30^\circ$ and $\theta = -90^\circ$, with the net lateral force being $\approx 28.8\%$ and $\approx 30\%$ of the net normal force, respectively. Additionally, there is a consistent ratio for the anomalous case within the range of -45° to -15° , followed by a significant change outside that range. Flat regions on the curve indicate ranges where the angle of incidence will not be a crucial factor to the net force ratios. This is an important aspect of metasurface design to consider when choosing a phase gradient that is consistent over a large range of incidence angles. These values will change depending on the anomalous reflection conversion efficiency as well, which will be discussed later.

Nevertheless, an effective way to optimize the lateral-to-normal force ratio of the solar sail is a significant development in metasurface-based attitude control. While rigorous analysis of metasurface placement on the solar sail surface will be carried out in a later section, we would like to note that in order for there to be a significant torque along the roll axis of the sail,

metasurfaces would ideally be placed a distance away from the center of the sail. This would increase the moment arm, and therefore the torque. In this case, any normal force components would also contribute to a torque along the pitch and yaw axes of the sail as well, which may be undesirable. In order to minimize this effect, it is important to know the optimal angle that produces the largest lateral force in relation to the normal force for a particular metasurface. Our results from Figure 2.6c indicate large peaks in this ratio at an incidence angle of -90° , which increase for smaller values of ζ . The significance of the results presented can be efficiently realized by designing a metasurface to produce a larger torque along the roll axis in relation to the yaw and pitch axes. However, as $\zeta \rightarrow 0$, the slope becomes steeper, to the point that the incident angle must essentially be exactly -90° , which is parallel incidence and not physically realizable.

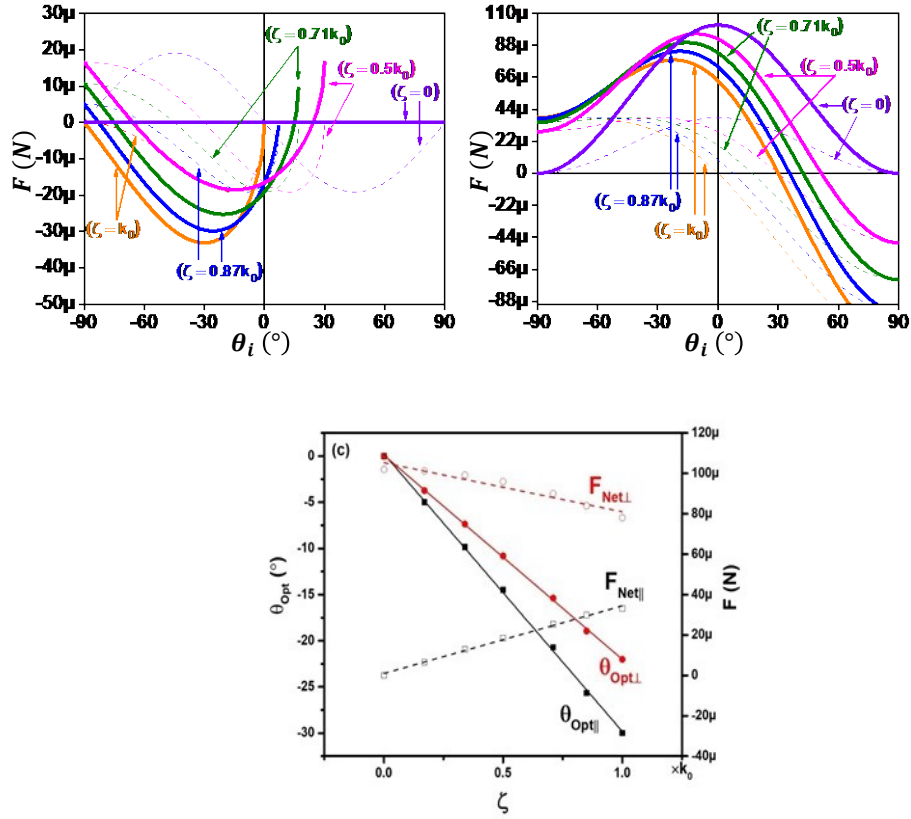


Figure 2.7 (a) is a plot of the anomalous reflection force (dashed), and net force (bold green) for the lateral components of the solar sail at different phase gradients. (b) is the same, but for the normal components. (c) is the optimal angle that produces the largest magnitude net force for both lateral (black) and normal (red) cases as a function of the phase gradient. All plots have the parameter, $\eta_{anom} = 0.75$.

To further examine the effect a metasurface phase gradient has on the force on a solar sail, Figure 2.7 shows the anomalous reflection forces and net forces on the solar sail for different phase gradients. For the lateral forces, as shown in Figure 2.7a, a phase gradient of k_0 will create the maximum net lateral force, and a phase gradient of zero will cause the net force to be zero, which is the appropriate result since $\zeta = 0$ is equivalent to purely specular reflection. Figure 2.7b shows the normal forces on the solar sail for comparison. A phase gradient of zero,

which corresponds with specular reflection, reaches a maximum net force at normal incidence as expected. As the phase gradient increases, the net normal forces slowly decrease, and with a phase gradient k_0 , the lowest net force is produced.

Figure 2.7c plots the angles that produce the largest net force for each phase gradient and the corresponding forces. The black squares and red circles represent the normal and lateral forces respectively. The solid black lines and symbols correspond to the optimal angles, while the hollow symbols and dashed lines correspond with the optimal forces at these angles. During solar sail missions, it will typically be important for any attitude adjustments to maintain maximum thrust in both lateral and normal trajectories. The angle where both normal and lateral net forces have the same optimal angle correspond only to metasurfaces with $\zeta = 0$, and an angle of incidence of 0° . It shows that the larger the phase gradient for the metasurface becomes, the more decoupled the optimal angles for the normal and lateral net forces will be. Therefore, a balance will need to be maintained in order to allow for the greatest possible net lateral force (which occurs when ζ is large), and consistency between normal and lateral optimal angles (which occurs when ζ is small). This result is particularly important when the desired response is not a net torque, but rather a translational motion of the solar sail system.

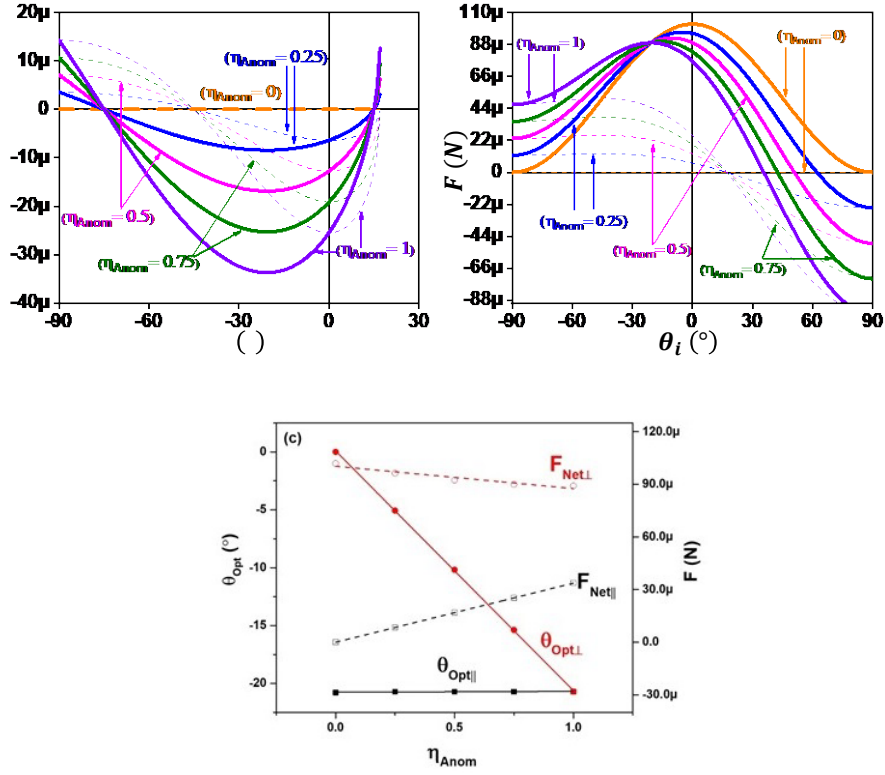


Figure 2.8 (a) is a plot of the anomalous reflection force (dashed), and net force (bold green) for the lateral components of the solar sail at different values of anomalous conversion efficiency. (b) is the same, but for the normal components. (c) is the optimal angle that produces the largest magnitude net force for both lateral (black) and normal (red) cases as a function of the anomalous conversion efficiency. All plots have the parameter $\zeta = 0.71k_0$.

In the next study, we examine the effect of the anomalous conversion efficiency on the forces. Most metasurfaces designed for anomalous reflection have not yet been able to achieve 100% conversion efficiency. A larger anomalous conversion efficiency means that there is more anomalous reflection, which is crucial for producing lateral forces on the sail. Figure 2.8a supports this claim, as the largest lateral net force occurs when 100% of the incident light is converted into anomalous reflections, and no lateral net force is generated when $\eta_{\text{anom}} = 0$. Following suit, Figure 2.8b shows that the greatest normal force occurs when the anomalous

conversion efficiency is 0%, and the least normal force occurs when it is 100%. Once again, the angles that produce the maximum net forces are examined in Figure 2.8c, with respect to the anomalous reflection efficiency. From Figure 2.8a and 2.8c, it should be noted that for the lateral forces, the maximum net forces are all at the same angle, with only the magnitude of the net force changing with anomalous reflection efficiency. For the normal case in Figure 2.8b and Figure 2.8c, it can be seen that the optimal angle changes linearly with the anomalous reflection efficiency. The point where both the normal and lateral optimal angles are the same is at an anomalous reflection efficiency of 100%. Once again, this parameter can be taken into consideration when choosing metasurfaces to be further designed and utilized. An ideal case would have $\eta_{anom} = 1$.

The derivations we have done so far are a vital first step to understanding how metasurfaces could be used with solar sails. We have shown that anomalous reflections from metasurfaces can indeed be used to create tangential forces, and therefore to alter the attitude of a solar sail. Additionally, the metasurfaces would be able to create a net torque along the roll axis of the sail, particularly if they were positioned along the edge of the sail. Metasurfaces can be designed to produce a constant phase gradient that corresponds to the largest magnitude tangential force. From our plots, this phase gradient was found to be $\zeta = k_0$. Additionally, we have developed a method to determine the optimum angles to maximize the magnitude of the lateral force on the solar sail in relation to the normal force. For a solar sail system with a metasurface having $\eta_{anom} = 0.75$ and $\zeta = 0.71k_0$, there are two optimal angles that produce the largest net lateral-to-normal force ratio. The first angle ($\approx 28.8\%$ of the net normal force) would be at -30° , and the second ($\approx 30\%$ of the net normal force) is at -90° . For decreasing magnitudes of constant phase gradient, the local maximum of the lateral-to-normal ratio

increases significantly, though at the expense of approaching a physically unrealizable incidence angle. Finally, we found that for different values of ζ , there are ranges of fairly constant lateral-to-normal ratios that can be chosen while picking metasurface phase gradients to use on solar sails. Very small, nonzero, phase gradients have the longest ranges of constant normal-to-lateral ratios, with the added benefit that they have very large maximas approaching $\theta = -90^\circ$. This means that they will behave closely to specular reflectors for most incidence angles, and then be able to exhibit very high lateral force at grazing incidences. This work therefore demonstrates the high potential of anomalously reflected light from a metasurface for solar sail control to generate torque along the roll axis of a solar sail.

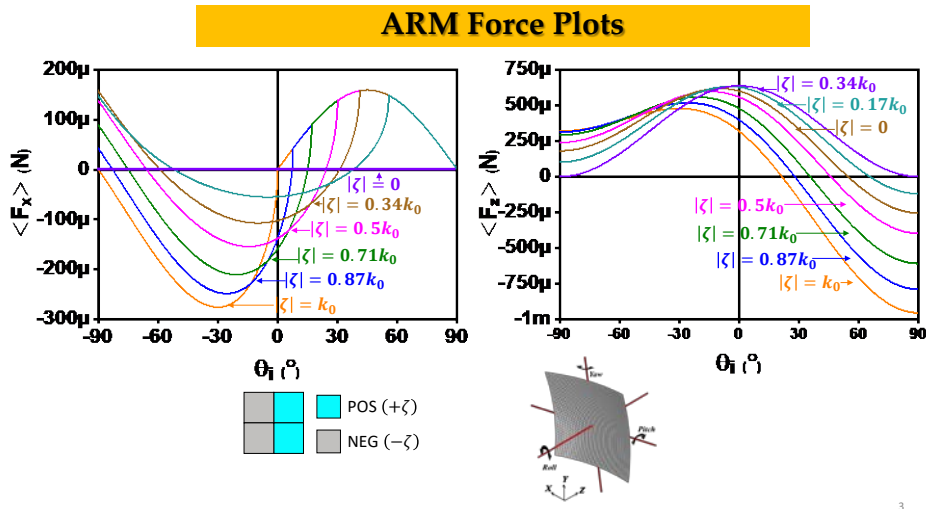


Figure 2.9 Plots of the net normal and lateral forces from anomalously reflecting metasurfaces for varying phase gradients, ζ . Both plots exhibit a scenerio where the metasurface anomalous conversion efficiency, η_{anom} , is 100%.

Figure 2.9 displays the forces on the solar sail when half of the sail has a certain phase gradient, and the other half has the same phase gradient, but with an opposite sign. The figures are consistent with the previous ARM force plots by the fact that a phase gradient of zero

produces the largest normal force, while also producing zero lateral force. Additionally, Fig 2.9 displays the value for the force equation across the entire range of -90° to 90° . The previous ARM plots only showed the values that did not contain any imaginary part, while this plot shows the real value of all force terms, even if the solution is complex.

CHAPTER 3. DERIVATION OF TORQUES

To begin, I will first derive the equations for the torque on a solar sail in the case of a purely specularly reflecting solar sail.

$$\mathbf{r} = x \hat{\mathbf{x}} + y \hat{\mathbf{y}} + z \hat{\mathbf{z}} \quad (3.1)$$

$$\boldsymbol{\tau} = \int \mathbf{r} \times d\mathbf{F} dS = \int_{-L_y}^{L_y} \int_{-L_x}^{L_x} \mathbf{r} \times d\mathbf{F} dx dy \quad (3.2)$$

$$\begin{aligned} \tau_x = \int_{-L_y}^{L_y} \int_{-L_x}^{L_x} & -\frac{P y \cos(\theta)}{\epsilon_b + \epsilon_f} \left(\epsilon_b \left((\rho - 1) B_b - \rho(s - 1) B_f + \cos(\theta) (s + 1) \right) \right. \\ & \left. + \epsilon_f (-s B_f + B_f + \cos(\theta) + s \cos(\theta)) \right) dx dy = 0 \end{aligned} \quad (3.3)$$

$$\begin{aligned} \tau_y = \int_{-L_y}^{L_y} \int_{-L_x}^{L_x} & \frac{P x \cos(\theta)}{\epsilon_b + \epsilon_f} \left(\epsilon_b \left((\rho - 1) x B_b - \rho(s - 1) x B_f + x \cos(\theta) (s + 1) \right) \right. \\ & \left. + (\rho - 1)(-z) \sin^2(\theta) \right) \\ & \left. + \epsilon_f \left(B_f(x - sx) + x \cos(\theta) (s + 1) + (\rho - 1)(-z) \sin^2(\theta) \right) \right) dx dy = 0 \end{aligned} \quad (3.4)$$

$$\tau_z = \int_{-L_y}^{L_y} \int_{-L_x}^{L_x} P y (\rho - 1) \sin^2(\theta) \cos(\theta) dx dy = 0 \quad (3.5)$$

For the case of a flat, uniform solar sail with the center of mass and the center of pressure in the center of the sail, there is no torque along any of the principal axes.

3.1 Torque from Reflection Control Devices

In that same way that we integrated all of the force elements across the solar sail with different sections having different optical properties, the same will be done when calculating the torque. In this case, however, the cross product of each position vector will be taken with each differential force element before being integrated over the surface of each discrete section. The same five different geometric configurations are considered for the following torque calculations (case 1 was covered earlier in the general torque derivation for a uniform solar sail).

$$\text{Case 2: } \begin{pmatrix} 1 & 0 \\ 1 & 0 \end{pmatrix}$$

$$\begin{aligned} \boldsymbol{\tau} &= \int_0^{L_y} \int_{-L_x}^0 \mathbf{r} \times d\mathbf{F}(s_{ON}) dx dy + \int_0^{L_y} \int_0^{L_x} \mathbf{r} \times d\mathbf{F}(s_{OFF}) dx dy + \int_{-L_y}^0 \int_{-L_x}^0 \mathbf{r} \times d\mathbf{F}(s_{ON}) dx dy \\ &\quad + \int_{-L_y}^0 \int_{-L_x}^0 \mathbf{r} \times d\mathbf{F}(s_{OFF}) dx dy \\ &= L_x L_y P \cos(\theta) \left(L_x \rho B_f (s_{ON} - s_{OFF}) + L_x \rho (s_{OFF} - s_{ON}) \cos(\theta) \right. \\ &\quad \left. - 4(\rho - 1)z \sin^2(\theta) \right) \hat{\mathbf{y}} \end{aligned} \tag{3.6}$$

$$\text{Case 3: } \begin{pmatrix} 1 & 1 \\ 0 & 0 \end{pmatrix}$$

$$\begin{aligned} \boldsymbol{\tau} &= \int_0^{L_y} \int_{-L_x}^0 \mathbf{r} \times d\mathbf{F}(s_{ON}) dx dy + \int_0^{L_y} \int_0^{L_x} \mathbf{r} \times d\mathbf{F}(s_{OFF}) dx dy + \int_{-L_y}^0 \int_{-L_x}^0 \mathbf{r} \times d\mathbf{F}(s_{ON}) dx dy \\ &\quad + \int_{-L_y}^0 \int_{-L_x}^0 \mathbf{r} \times d\mathbf{F}(s_{OFF}) dx dy \\ &= L_x L_y^2 P \rho \cos(\theta) (s_{OFF} - s_{ON}) (\cos(\theta) - B_f) \hat{\mathbf{x}} \\ &\quad - 4L_x L_y P (\rho - 1) z \sin^2(\theta) \cos(\theta) \hat{\mathbf{y}} \end{aligned} \tag{3.7}$$

Case 4: $\begin{pmatrix} 1 & 0 \\ 0 & 1 \end{pmatrix}$

$$\begin{aligned}
\boldsymbol{\tau} &= \int_0^{L_y} \int_{-L_x}^0 \mathbf{r} \times d\mathbf{F}(s_{ON}) dx dy + \int_0^{L_y} \int_0^{L_x} \mathbf{r} \times d\mathbf{F}(s_{OFF}) dx dy + \int_{-L_y}^0 \int_{-L_x}^0 \mathbf{r} \times d\mathbf{F}(s_{ON}) dx dy \\
&\quad + \int_{-L_y}^0 \int_{-L_x}^0 \mathbf{r} \times d\mathbf{F}(s_{OFF}) dx dy \\
&= -4L_x L_y P(\rho - 1) z \sin^2(\theta) \cos(\theta) \hat{\mathbf{y}}
\end{aligned} \tag{3.8}$$

Case 5: $\begin{pmatrix} 1 & 1 & 1 & 1 \\ 1 & 1 & 1 & 0 \\ 1 & 1 & 0 & 0 \\ 1 & 0 & 0 & 0 \end{pmatrix}$

$$\begin{aligned}
\boldsymbol{\tau} = & \int_{\frac{L_y}{2}}^{L_y} \int_{-L_x}^{-\frac{L_x}{2}} \mathbf{r} \times d\mathbf{F}(s_{on}) dx dy + \int_{\frac{L_y}{2}}^{L_y} \int_0^{-\frac{L_x}{2}} \mathbf{r} \times d\mathbf{F}(s_{on}) dx dy + \int_{\frac{L_y}{2}}^{L_y} \int_0^{\frac{L_x}{2}} \mathbf{r} \times d\mathbf{F}(s_{on}) dx dy \\
& + \int_{\frac{L_y}{2}}^{L_y} \int_{\frac{L_x}{2}}^{L_x} \mathbf{r} \times d\mathbf{F}(s_{on}) dx dy + \int_0^{\frac{L_y}{2}} \int_{-L_y}^{-\frac{L_x}{2}} \mathbf{r} \times d\mathbf{F}(s_{on}) dx dy \\
& + \int_0^{\frac{L_y}{2}} \int_0^{-\frac{L_x}{2}} \mathbf{r} \times d\mathbf{F}(s_{on}) dx dy + \int_0^{\frac{L_y}{2}} \int_{L_x}^{\frac{L_x}{2}} \mathbf{r} \times d\mathbf{F}(s_{on}) dx dy \\
& + \int_0^{\frac{L_y}{2}} \int_{\frac{L_x}{2}}^{L_x} \mathbf{r} \times d\mathbf{F}(s_{off}) dx dy + \int_{-\frac{L_y}{2}}^0 \int_{-L_x}^{-\frac{L_x}{2}} \mathbf{r} \times d\mathbf{F}(s_{on}) dx dy \\
& + \int_{-\frac{L_y}{2}}^0 \int_0^{-\frac{L_x}{2}} \mathbf{r} \times d\mathbf{F}(s_{on}) dx dy + \int_{-\frac{L_y}{2}}^0 \int_0^{\frac{L_x}{2}} \mathbf{r} \times d\mathbf{F}(s_{off}) dx dy \\
& + \int_{-\frac{L_y}{2}}^0 \int_{\frac{L_x}{2}}^{L_x} \mathbf{r} \times d\mathbf{F}(s_{off}) dx dy + \int_{-L_y}^{-\frac{L_y}{2}} \int_{-L_x}^{-\frac{L_x}{2}} \mathbf{r} \times d\mathbf{F}(s_{on}) dx dy \\
& + \int_{-L_y}^{-\frac{L_y}{2}} \int_0^{-\frac{L_x}{2}} \mathbf{r} \times d\mathbf{F}(s_{off}) dx dy + \int_{-L_y}^{-\frac{L_y}{2}} \int_0^{\frac{L_x}{2}} \mathbf{r} \times d\mathbf{F}(s_{off}) dx dy \\
& + \int_{-L_y}^{-\frac{L_y}{2}} \int_{\frac{L_x}{2}}^{L_x} \mathbf{r} \times d\mathbf{F}(s_{off}) dx dy \\
& = \frac{5}{8} L_x L_y^2 P \rho \cos(\theta) (s_{off} - s_{on}) (\cos(\theta) - B_f) \hat{\mathbf{x}} \\
& + \frac{1}{8} L_x L_y P \cos(\theta) \left(5L_x \rho B_f (s_{on} - s_{off}) + 5L_x \rho \cos(\theta) (s_{off} - s_{on}) - 32(\rho - 1) z \sin^2(\theta) \right) \hat{\mathbf{y}} \quad (3.9)
\end{aligned}$$

Figure 3.1, 3.2 and 3.3 show the plots of the normal and tangential torque components on the solar sail from varying different optical properties of the solar sail. Once again, the main point of the following plots is for a point of comparison between the next set of derivations for the torque due to anomalously reflecting metasurfaces. Figure 3.3, has no torque along the roll axis.

RCD Torque Plots Varying Transmission

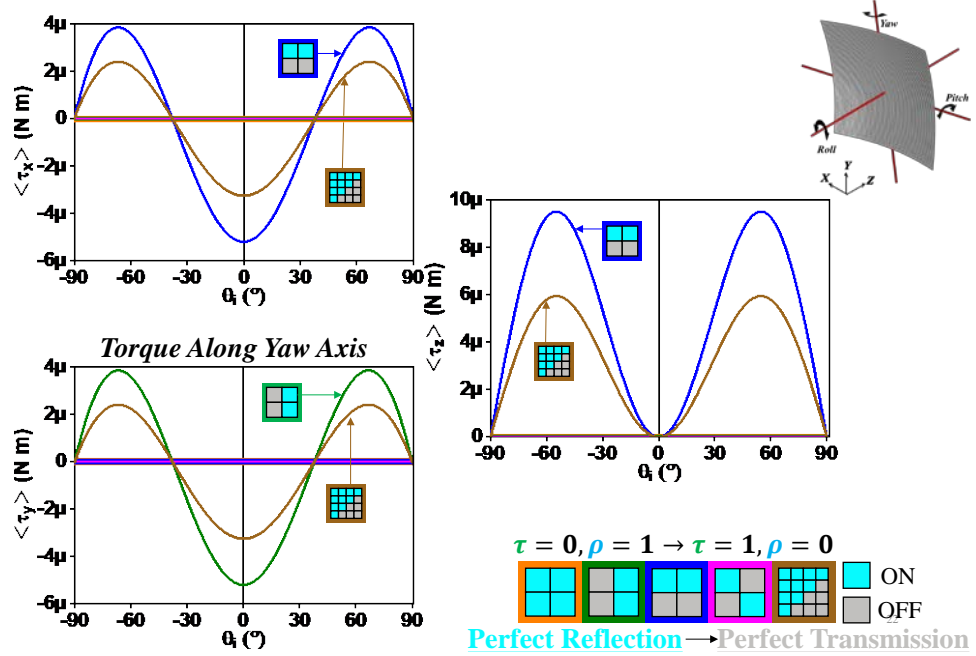


Figure 3.1 x (pitch), y (yaw) and z (roll) components of torque on the solar sail using tunable transmission RCDs.

RCD Torque Plots Varying Absorption/Emission

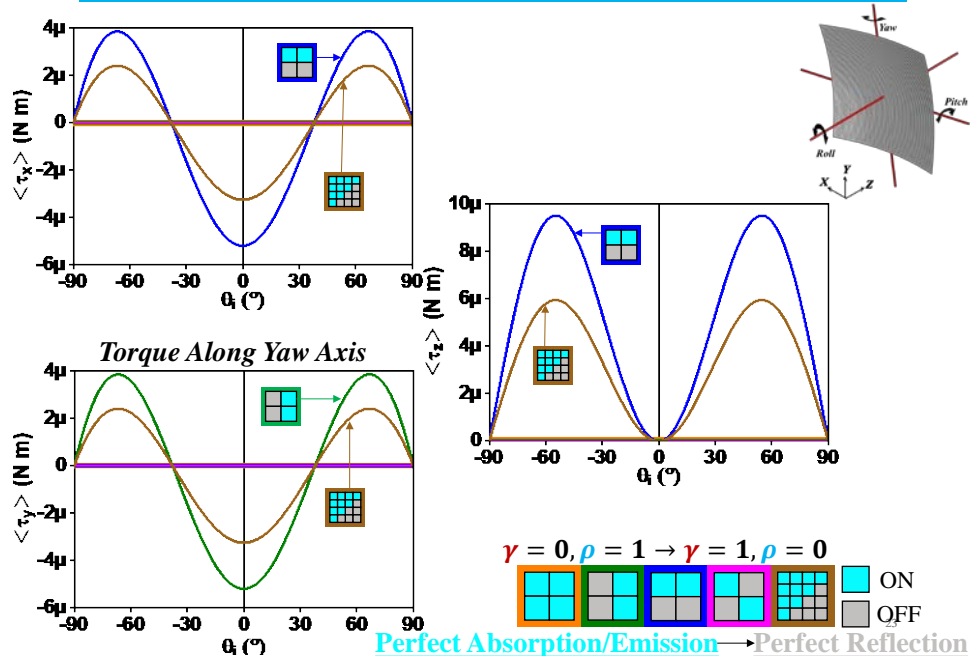


Figure 3.2 x (pitch), y (yaw) and z (roll) components of torque on the solar sail using tunable absorption/emission RCDs.

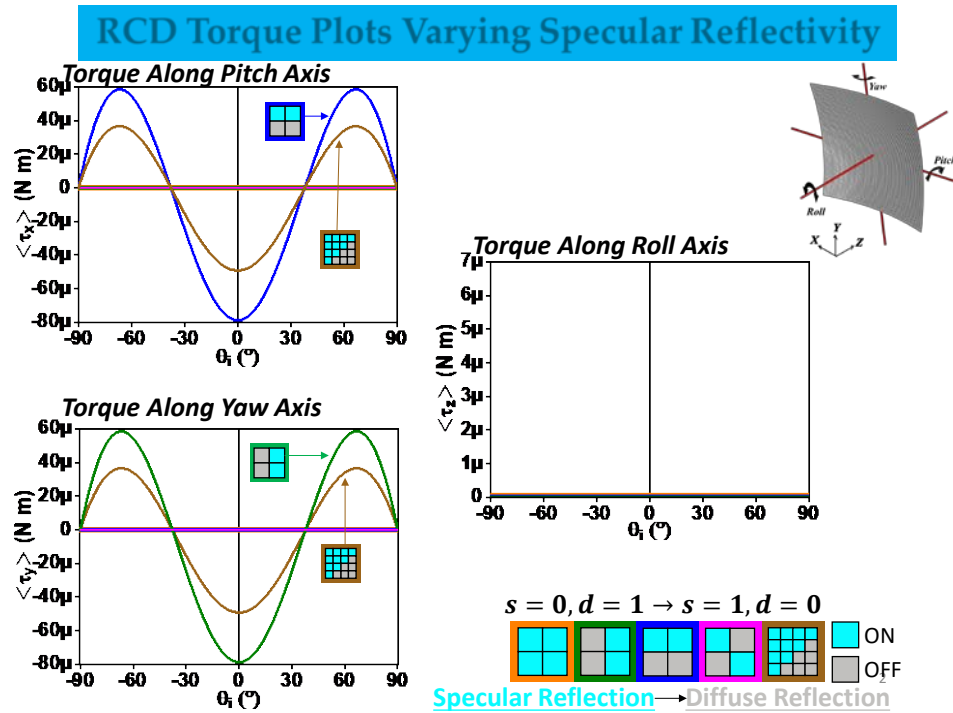


Figure 3.3 x (pitch), y (yaw) and z (roll) components of torque on the solar sail using tunable specular reflection.

3.2 Torque from Anomalous Reflections

To allow for easy visualization of the effect the metasurfaces would have on a solar sail, we developed some models in COMSOL to generate the force and torque vectors at each individual location along the surface of a sail with respect to a specified point of pivot. These models will be valuable to identify the ideal locations to distribute the metasurfaces, in addition to simulating the overall solar sail response. Flat, square solar sail, and curved solar sail models were generated. The overall torque along each axes of rotation (pitch, yaw and roll) could be found by adding together all of the torque vectors over the surface of the sail. We could then compare the theoretical torque values that would arise from utilizing the proposed metasurfaces to reported data on real-life solar sail missions and publications, such as the NEA Scout. The

torque along the roll axis can then be found by crossing each position vector \mathbf{r} , from the center point on the sail to a given sail element, with each corresponding differential element of force and adding up all of the contributions [22].

$$\boldsymbol{\tau}_{net} = (\langle dF_z \rangle y - \langle dF_y \rangle z) \hat{\mathbf{x}} + (\langle dF_x \rangle z - \langle dF_z \rangle x) \hat{\mathbf{y}} + (\langle dF_y \rangle x - \langle dF_x \rangle y) \hat{\mathbf{z}} \quad (3.10)$$

Since there is no y component of force, the torque along the roll axis comes out to be,

$$\begin{aligned} \langle \tau_z \rangle = \int_S \langle dF_y \rangle x - \langle dF_x \rangle y \, dS = & -\frac{\mu_0 E_0^2}{2\eta_0^2} \left(\sin(\theta) \cos(\theta) - \frac{\zeta + k_0 \sin(\theta)}{k_0} \sqrt{1 - \left(\sin(\theta) + \frac{\zeta}{k_0} \right)^2} \right) \\ & \times \int_{-\frac{L_x}{2}}^{\frac{L_x}{2}} \int_{-\frac{L_y}{2}}^{\frac{L_y}{2}} y \, dy \, dx. \end{aligned} \quad (3.11)$$

Since the above integral will be zero if the metasurface is symmetric about the y-axis, it will be necessary to include metasurfaces with different values of ζ to break the symmetry.

Ideally, metasurfaces with phase gradients that are of equal and opposite signs would be on either side of the y-axis. This could be achieved by a gradient metamaterial structure rotated 180° with respect to its counterpart. If this is the case, the new, optimized torque, $\tau_{z,opt}$, can be found to be,

$$\begin{aligned} \langle \tau_{z,opt} \rangle = \frac{\mu_0 E_0^2 L_x L_y^2 \eta_{anom}}{16\eta_0^2 k_0} & \left((\zeta_+ + k_0 \sin(\theta)) \sqrt{1 - \left(\sin(\theta) + \frac{\zeta_+}{k_0} \right)^2} \right. \\ & \left. - (\zeta_- + k_0 \sin(\theta)) \sqrt{1 - \left(\sin(\theta) + \frac{\zeta_-}{k_0} \right)^2} \right) \end{aligned} \quad (3.12)$$

Due to the time-varying nature of the sail system, in future investigations it will be important to investigate dynamically tunable methods to either turn off and on the anomalous reflections, or actively vary the phase gradient of the metasurfaces.

In the same way, the pitch and yaw torques can be found from the derived forces.

$$\begin{aligned} \langle \tau_x \rangle &= \int_S \langle dF_z \rangle y - \langle dF_y \rangle z dS \\ &= \frac{E_0^2 L_x L_y}{2\eta_0^2 k_0^2} (\mu_0 (k_0^2 \cos(2\theta) - \zeta \eta_{\text{anom}} (\zeta + 2k_0 \sin(\theta))) + \eta_0^2 k_0^2 \epsilon_0) \int_{-\frac{L_x}{2}}^{\frac{L_x}{2}} \int_{-\frac{L_y}{2}}^{\frac{L_y}{2}} y dy dx. \end{aligned} \quad (3.13)$$

$$\begin{aligned} \langle \tau_y \rangle &= \int_S \langle dF_x \rangle z - \langle dF_z \rangle x dS \\ &= \int_{-\frac{L_x}{2}}^{\frac{L_x}{2}} \int_{-\frac{L_y}{2}}^{\frac{L_y}{2}} \frac{E_0^2 L_x L_y}{2\eta_0^2 k_0^2} (\mu_0 (\eta_{\text{anom}} (k_0 (k_0 z \sin(\theta) (\cos(\theta) - \varrho) + 2\zeta x \sin(\theta) \\ &\quad + \zeta(-z)\varrho) + \zeta^2 x) - k_0^2 x \cos(2\theta)) - \eta_0^2 k_0^2 x \epsilon_0) dy dx, \end{aligned} \quad (3.14)$$

where,

$$\varrho = \sqrt{\cos^2(\theta) - \frac{\zeta}{k_0^2} (\zeta + 2k_0 \sin(\theta))}. \quad (3.15)$$

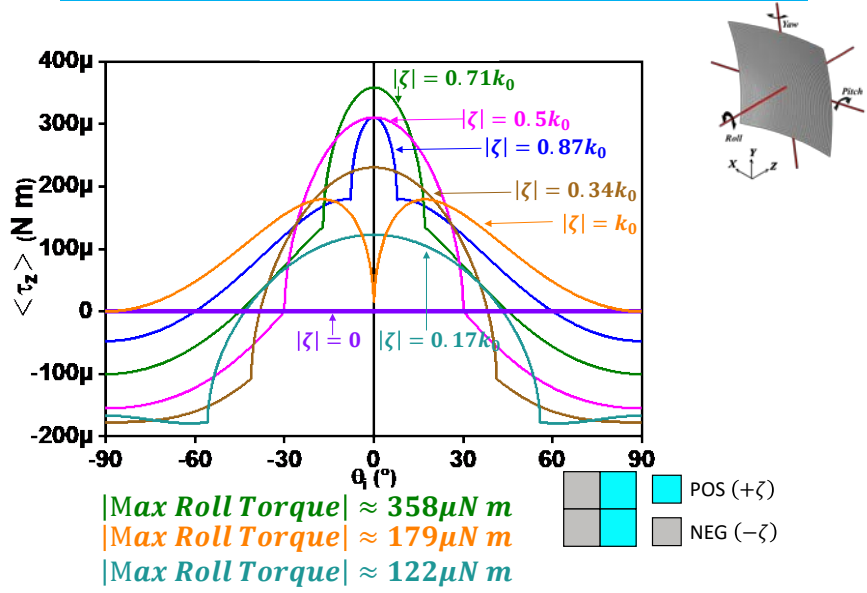
The integrals above also equal zero, so there is no net torque on the solar sail system if the metasurface is uniform across the whole surface. The net torque along the pitch and yaw axes corresponding to the metasurface configuration which gives rise to the greatest magnitude of roll torque can be found by integrating under the same conditions as before,

$$\langle \tau_{x,opt} \rangle = - \frac{E_0^2 \mu_0 \eta_{\text{anom}} (\zeta_+ - \zeta_-) L_x L_y^2 (\zeta_+ + \zeta_- + 2k_0 \sin(\theta))}{16\eta_0^2 k_0^2} \quad (3.16)$$

$$\begin{aligned}
\langle \tau_{y,opt} \rangle = & -\frac{(E_0^2 \mu_0 z L_x L_y)}{4\eta_0^2 k_0} \left(\sqrt{1 - \left(\sin(\theta) + \frac{\zeta_+}{k_0} \right)^2} (\zeta_+ \eta_{anom} + k_0 \eta_{anom} \sin(\theta)) \right. \\
& \left. + \sqrt{1 - \left(\sin(\theta) + \frac{\zeta_-}{k_0} \right)^2} (\zeta_- \eta_{anom} + k_0 \eta_{anom} \sin(\theta)) - k_0 \eta_{anom} \sin(2\theta) \right).
\end{aligned}
\tag{3.17}$$

Figure 3.4 show the plots of the normal and tangential torque components on the solar sail for varying values of phase gradient, ζ . The roll torque from anomalous reflections can reach a maximum of $358\mu N m$, which is a drastic increase from the previous cases that utilized RCDs. There is an increase by at least two orders of magnitude in roll torque for the ARM compared to the RCD cases.

ARM Torque Plots



ARM Torque Plots

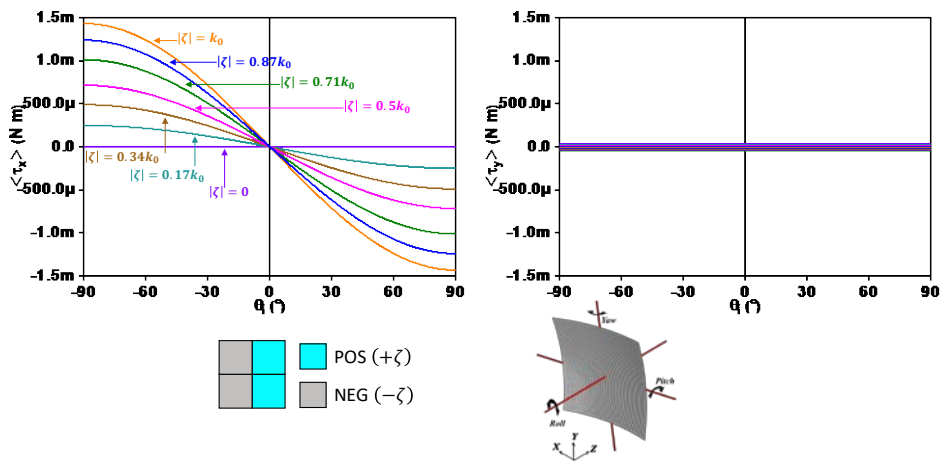


Figure 3.4 Torque along the pitch and yaw axes respectively. Both cases exhibit 100% anomalous efficiency ($\eta_{Anom} = 1$).

CHAPTER 4. MANUFACTURE AND CHARACTERIZATION

Before outlining the proposed future research plan, we will begin by summarizing some of the work that has been done over the course of the last two years. We have made significant progress in the analysis of metasurfaces and identifying possible methods of manufacture, while also continuing to adapt and improve our research plan in order to maximize the development of this important technology so that it can be utilized in future space missions.

The scope of our research plan was altered upon the realization of an improved method of attitude control. Originally, the plan had been to utilize the tunable Fermi energy of graphene-based devices, though this concept could be taken a step further with the utilization of anomalously reflecting metasurfaces. Ultimately, the new research plan will add a whole other dimension of attitude control freedom allowing for manipulation of the torque about the roll-axis of the sail, in addition to the pitch and yaw axes that were the primary focus when considering the 2-D metamaterial reflectivity-control devices. Outlined below is some of the methods and procedures we have considered for manufacturing the proposed attitude control devices. While graphene would have been a good candidate for a reflection control device due to the fact that its reflection could be tuned thanks to its stunnable Fermi energy, graphene can also be used for a metasurface as well. It is for this reason that we have taken a keen interest in developing an effective method to produce graphene on a large scale.

4.1 Production of Graphene

Graphene is a very useful and important material because of its many great properties. Graphene has great mechanical strength, making it useful for applications that need improved strength. Additionally, it has great conductivity, which is also very important. It has even higher conductivity than copper, which means that it would be very useful to develop an effective means to produce a ready supply of graphene for whatever the application is required.

To do this, however, it is important to be able to understand exactly what graphene is, or more importantly, what it makes up. Graphene is a single layer of bulk graphite. When stacked on top of each other, the layers of graphene bond and the bulk substance is called graphite. Graphite is a commonly available material and, despite the fact that it is made up of graphene layers, it has significantly less useful properties compared with monolayer graphene.

The mechanical strength, in particular, is significantly reduced. Graphite is a relatively soft and brittle material, while graphene is supposed to have the best recorded tensile strength of any known material as of present. This is partly because, while the covalent bonds between the carbon atoms in the 2D graphene lattice are very strong, the van der Waal bonds that bond the layers of graphene on top of each other are much weaker in comparison. This crucial detail must be exploited when trying to convert bulk graphite into monolayer graphene sheets [23][24][25].

4.1.1. Exfoliation/Cleavage

One of the early methods for creating graphene from bulk graphite was as simple as using scotch tape to peel away the layers of graphite. After enough times of applying tape and peeling away layers, eventually it was recorded that single layer graphene could be found. Despite being a fairly unsophisticated method, micromechanical cleavage did the job, and was one of the first instances where graphene was created.

This method has some drawbacks though, particularly in the fact that it is not very scalable, and it is not effective for mass production of graphene. Additionally, finding flakes of monolayer graphene is an inconsistent process, and typically involves manually scanning through a sample until you find single layer flakes amongst all of the multilayer flakes and/or bulk graphite layers [25].

A slightly more modern method, and one that is very commonly utilized, is liquid phase exfoliation. Instead of using mechanical forces, such as force of the tape on the graphite, this method uses sound to break apart the graphite layers. The ultrasonic frequencies can be produced by a bath or probe sonicator. The probe sonicator uses a piezoelectric tip attached to a probe, which will produce ultrasonic acoustic waves. The probe sonicator is generally the more powerful sonication method, and samples usually require less sonication time when prepared in this manner

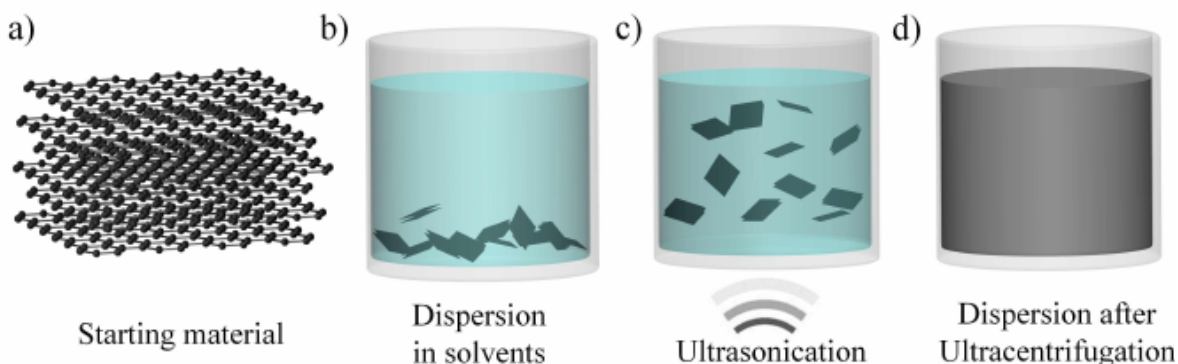


Figure 4.1 Schematic diagram of the various stages of liquid phase exfoliation via sonication [26].

The first step in liquid phase exfoliation is to mix bulk graphite powder into solutions, such as N-Methyl-2-Pyrrolidone (NMP), that can weaken the van der Waal bonds of the graphite without disturbing the covalent bonds within the graphene honeycomb lattice. When the solution

is being sonicated, the ultrasonic frequencies interact with the carbon layers, and break apart the van der Waal bonds by cavitation between the layers. When the solution has been sonicated, there will typically be particles of varying size and number of layers. A method to separate the bigger chunks of graphite/graphene is to place the solution in a centrifuge, which will rapidly spin the solution at high speeds. The larger chunks of the sample will gather on the side of the test tube, while the smaller chunks, which would ideally have many single layer graphene flakes, will remain disbursed in the solution. The solution can then be extracted with a pipette, leaving the larger chunks still impacted onto the test tube.

Some of the major benefits of this method are that it is a relatively simple and straightforward process, and it allows for large scalability. One disadvantage of this method, however, is that the process of sonication can break apart the graphene lattice, and create spacing between flakes. The more spaces there are between flakes, the higher the chance that the conductivity of the graphene sample will be negatively affected [26].

A less common method, that seems to show promise, is the process of microfluidization. This process boasts a very high reported conversion percentage of bulk graphite to graphene. The method consists of feeding a graphene solution into micro-chamber by means of a high-pressure intensifier pump. The microchambers act as an interaction chamber where the particles of the solution will collide with each other, before moving on to a cooling reservoir. The interaction chamber is reported to apply a uniform shear force over the bulk graphite particles, with even more uniformity than that supplied by sonication methods. The resulting particles are graphene flakes. While this method seems to produce good results, it does require a very large intensifier pump [27].

A necessary task is to develop large-scale fabrication techniques for graphene. Chemical Vapor Deposition (CVD), mechanical exfoliation, chemical exfoliation and chemical synthesis are all methods that have been used for fabrication of graphene. We will evaluate methods that can be scalable to large areas. Graphene printing has been introduced as an alternative fabrication technique for producing graphene that does not have the same high temperature annealing processes as CVD. Graphene printing is a low-cost, viable technique that allows for the production of micropatternable graphene films. There are a variety of ways to create graphene ink, including commonly utilized techniques such as liquid-phase exfoliation and shear exfoliation. The disadvantages of these techniques are, despite the fact that they are much more scalable methods than CVD or mechanical exfoliation, a significant amount of graphite remains unexfoliated after the procedures. Additionally, sonication processes can take a considerable amount of time, even after utilizing expensive sonicator tips. While the method of fabrication for graphene may be liable to change, we feel that graphene printing is the best option because of the importance of large scalability. Graphene ink can be bought commercially from a company or made by a variety of processes. A novel technique called microfluidization has seemed to hold the most promise from recent literature for producing scalable graphene layers. The process of exfoliation of graphite involves the weakening the Van der Waal bonds that hold the layers of graphene together in graphite, without disturbing the covalent bonds within the honeycomb lattice of the graphene layers. To do this, first an organic solvent is used to weaken the Van der Waal bonds. A solution of graphite and solvent begins in an inlet reservoir. A large pressure generated from an intensifier pump is then applied to the solution causing the liquid to be pulled into a channel less than 100 μ m in size. This initial step is preferable to the sonication procedures used during liquid-phase exfoliation because a high shear rate is applied uniformly over the

whole liquid, which does not happen during sonication. Once inside the microchambers, the graphite particles collide, creating shear forces that allow for uniform graphene production. There have been reports of exfoliation yields as high as 100%. Once the graphene is prepared, they can be mixed into an acrylic polymer binder system in order to gain the proper density, viscosity and surface tension for printing. The graphene ink can then be used in a commercially available inkjet printer for direct printing onto the appropriate, flexible substrate.

4.1.2. Epitaxial Growth/Chemical Vapor Deposition

Thermal chemical vapor deposition is a common preparation technique for high quality graphene. The graphene is grown directly onto a substrate by applying a hydrocarbon gas, and then heating it to high temperature in order to saturate the substrate with carbon. This method produces high quality graphene with few defects. Additionally, it is compatible with other Complementary Metal-Oxide-Semiconductor (CMOS) technology, which is an important factor when considering integration of the graphene with technology in the present industry. Some disadvantages of this method are that it is a relatively expensive procedure, and compared to other methods, such as the exfoliation methods, it is complex. Despite this, CVD remains one of the best methods for producing high quality graphene at the present day [28].

4.1.3. Thermal Decomposition On SiC:

Another simple method to implement is thermal decomposition of SiC onto a substrate. Similar to CVD, the monolayer of graphene is grown onto the substrate. The process is called vacuum graphitization, and it consists of applying a large heat to SiC gas, while the substrate-gas system is in a vacuum. The silicon will separate from the carbon, and the carbon will be left as a layer on the substrate. The layer of carbon can then be patterned using standard lithography methods. This method of graphene production produces graphene with very low defects, though

the graphene is discontinuous, as it forms into islands, which makes mass production difficult [25].

4.1.4. Chemically Derived Graphene

Graphene oxide is a widely considered alternative to graphene because it has many similar properties, while at the same time being much easier to mass-produce, while also being easier to disburse in water or other solutions. The major drawback of graphene oxide, however, is that while it has similar properties, it does not typically have the same great characteristics as pure graphene. There are methods that can help close the gap, however, which we will discuss further.

First, however, we will talk about the main method of producing graphene oxide. The method is called Hummer's method, and it entails oxidizing bulk graphite using a strong oxidizing agent. Oxidizing the graphite means that oxygen atoms will be bound between the van der Waal layers of the graphite, lengthening the separation between layers, and reducing the attractive force between the layers. This will allow the graphene layers to be easily separated in a manner similar to the liquid phase exfoliation method, by sonicating the oxidized graphite solution. The final result will be graphene oxide [24][29].

One method to improve the properties of graphene oxide is to remove as many of the oxygen functional groups that remain on the graphene oxide after sonication. The less oxygen functional groups, the closer the graphene oxide will be to pristine graphene, and the more likely the resulting reduced graphene oxide will have properties more comparable to pristine graphene.

There are three main ways of reducing graphene oxide, and they are via chemical, thermal and electrochemical methods [29].

Instead of removing the functional oxygen groups from the graphene oxide, it is also possible to improve the properties of the graphene oxide itself, without worrying about making it closer to pristine graphene. An example of a way that graphene oxide could be functionalized is by reducing the edge defects of the sample. The more edge defects there are, the less likely the graphene oxide will have a good conductivity, because there is more gaps in contact, which means more resistance. Sonication is a method that typically creates large edge defects because of the high-energy bombardment of the particles via ultrasonic acoustic waves. To reduce this, other methods besides sonication can be employed [30].

4.1.5. Graphene Classification and Identification

Spectroscopy is a common characterization technique for identifying graphene. While many useful properties can be obtained by spectroscopy, such as optical properties via Fourier transform spectroscopy, the main use for spectroscopy is to identify the graphene, and to evaluate the number of layers that are present on the sample. Raman spectroscopy is the most commonly used technique in this regard, and it measures the spectrum of the Raman scattering from the sample. Each material will have a unique spectrum, so in this regard Raman spectroscopy can be used to identify if the material is graphene. Additionally, the resonance peaks will be shifted based on the number of layers of graphene within the sample, which is another useful thing to know when attempting to create monolayer graphene [25][31].

Different microscopy techniques such as atomic force microscopy and transverse electron microscopy can be useful for obtaining morphological information about the graphene samples. Transverse electron microscopy in particular can be used for imaging and thickness detection. Additionally, it provides information on the frictional, electromagnetic and elastic properties of the graphene sample that is being measured [25].

The final characterization technique that we will discuss is related to measuring the electrical conductivity of the graphene. Since conductivity is such a useful property of graphene, this measurement is typically a crucial part of the graphene manufacturing process. A variety of methods can be used to measure conductivity, though the 4-probe method is one of the more common ones that is employed on a flat surface sample [25].

4.1.6. Discussion on Graphene

We have summarized a few graphene production methods and characterization techniques for evaluation purposes. We do not think that there is currently a single best method for all situations, and we think that choosing a production technique will depend on the situation. Currently, we think that CVD is one of the most reliable methods for consistently producing low-defect graphene, with the added benefit that the graphene produced will already be ready for integration with current CMOS technology. If a large amount of graphene (or graphene-like material) is required, then graphene oxide is the cheapest method for mass production. Graphene is highly versatile and useful material, therefore careful consideration must go into choosing a production method.

Graphene was the first two-dimensional (thickness <1 nm) material discovered, and has since been known for its exceptional electrical and mechanical properties. It is currently the strongest known material, with intrinsic tensile strength of 130 GPa [32]. Additionally, graphene exhibits high charge carrier mobility with measured values exceeding 1,000 cm/Vs [33]. A thermal conductivity between 1500–2500 $W(m \cdot K)^{-1}$ has also been reported for single layer graphene [34]. Graphene is also intrinsically flexible. For a long time, there had been much skepticism with concern to the existence of 2-D materials. It was thought that at that scale, 2D materials would be thermodynamically unstable. Reduced graphene oxide was first observed

with an electron microscope in 1962 [35]. Andrei Geim and Kostya Novoselov created monolayer graphene flakes from graphite in 2004 [36] While originally examining the electrical properties of bulk graphite, they eventually tried to make a sample thinner by using Scotch tape on a bulk block of graphite, and peeling away layers of graphite. After enough times, the layers of graphite were one atomic layer, making it graphene. After its discovery, there was a drastic jump in research efforts concerning graphene as the world came to understand the possible implications of such a material.

As part of our research, we planned to use graphene and other emerging 2D materials, such as semiconducting transition metal dichalcogenides, to design and engineer the ability to make the optical properties of metamaterials (e.g. reflectivity) electrically tunable while at the same time taking advantage of the ultra-thin and flexible characteristics of these 2D materials (thickness <1 nm).

In addition to the theoretical and analytical work we have done. We also worked with our group members on producing the graphene that could be used in the fabrication and testing of the metamaterial surface.

Using a liquid exfoliation method, we have been making progress developing a printable graphene ink, which can be used in any commercial inkjet printer [37][38][35][34][39][40][33]. Also, the method used to create the graphene ink could be easily adapted to other materials for future metamaterial fabrication. Liquid exfoliation was chosen because of the availability of equipment, cost of implementation, and overall final quality of the graphene [41][37][38][34].

Overall, our procedure consists of taking a sample of bulk graphite and mixing it with NMP in order to weaken the Van der Waal forces that hold the layers of graphene together [33][34][36]. Next, we sonicate the solution for ten minutes to fully disburse the graphene within

the solution, followed by centrifugation to help remove the bigger chunks of graphite. After extracting the supernatant, we use ethyl cellulose as an additive to help tailor the viscosity of the graphene solution to allow for proper extrusion from the printhead without any radial drops or “coffee rings.” Finally, we sonicate and centrifugate the new solution with the ethyl cellulose. We characterized the ink solution using Raman Spectroscopy in order to confirm that the Raman peaks were aligning with the expected values of graphene.

Additionally, we set up the printing system for graphene. Graphene powder is readily available in the lab, which will then need to be combined with an acrylic polymer binding system to make it have the correct viscosity and surface tension for inkjet printing.

The first step of this was to find a commercial inkjet printer that can be used with the graphene ink. Eventually we hope to be able to find an inexpensive roll-to-roll inkjet printer for large scalability, but for now, the available Epson Stylus NX530 and Canon Pixma IP4920 were sufficient for our purposes.

The next most important consideration for creating a graphene inkjet printing setup is to gather the materials needed to mix with the graphene in order to make the graphene powder usable as printer ink. From looking at previous literature on the subject of printing graphene using an inkjet printer, we found that graphene ink could be made by mixing graphene flakes with ethylene glycol and then ethyl cellulose as a stabilizer. 3% aqueous solution of hydrofluoric acid will also be used to keep the flake sizes of the graphene small enough so that they will easily fit through the diameter of the printing nozzle.

Once the graphene ink is prepared, we thoroughly washed out an ink cartridge and then used a syringe to inject the graphene ink into the clean cartridge. We can then print the graphene onto paper or some other substrate.

Throughout the academic semester, we have been working on developing a reliable means to print thin materials in commercial inkjet printers. This includes developing the inks, as well as formatting the printer and cartridge to allow for printing of these inks. Over the course of the fall semester, we have been able to continuously produce and characterize new graphene ink solutions with the goal of being able to print.

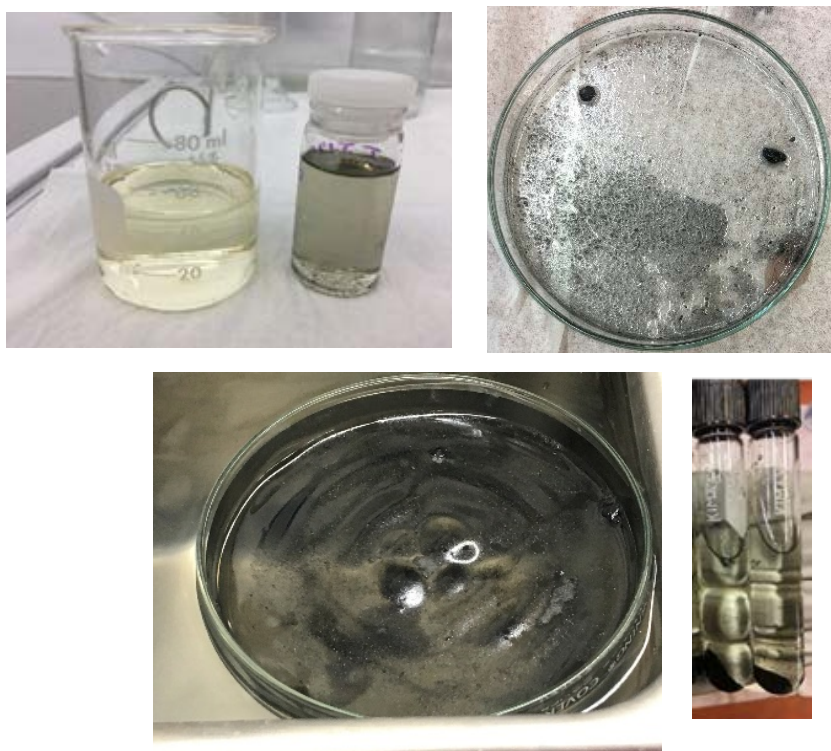


Figure 4.2 Images taken during the development process of the graphene ink. Large conglomerates of graphite chunks would accumulate in the petri dish after sonication (top right), The image on the bottom right is of the observed samples right after centrifugation. The sediment on the bottom of the tube contains larger chunks of graphene/graphite and is left behind after removing the supernatant.

Relatively good progress has been made with developing a usable ink that exhibits a Raman spectrum corresponding with monolayer graphene, but numerous setbacks have occurred relating to printer hardware. The initial Canon Pixma IP4920 printer broke down from electrical

problems that fried the printer's main logic board. Because of the Pixma's great printing resolution, multiple efforts were made to salvage the printer, though eventually it seemed that a better use of time would be continue working with another available printer model. We have since been working with the Epson Stylus NX430.

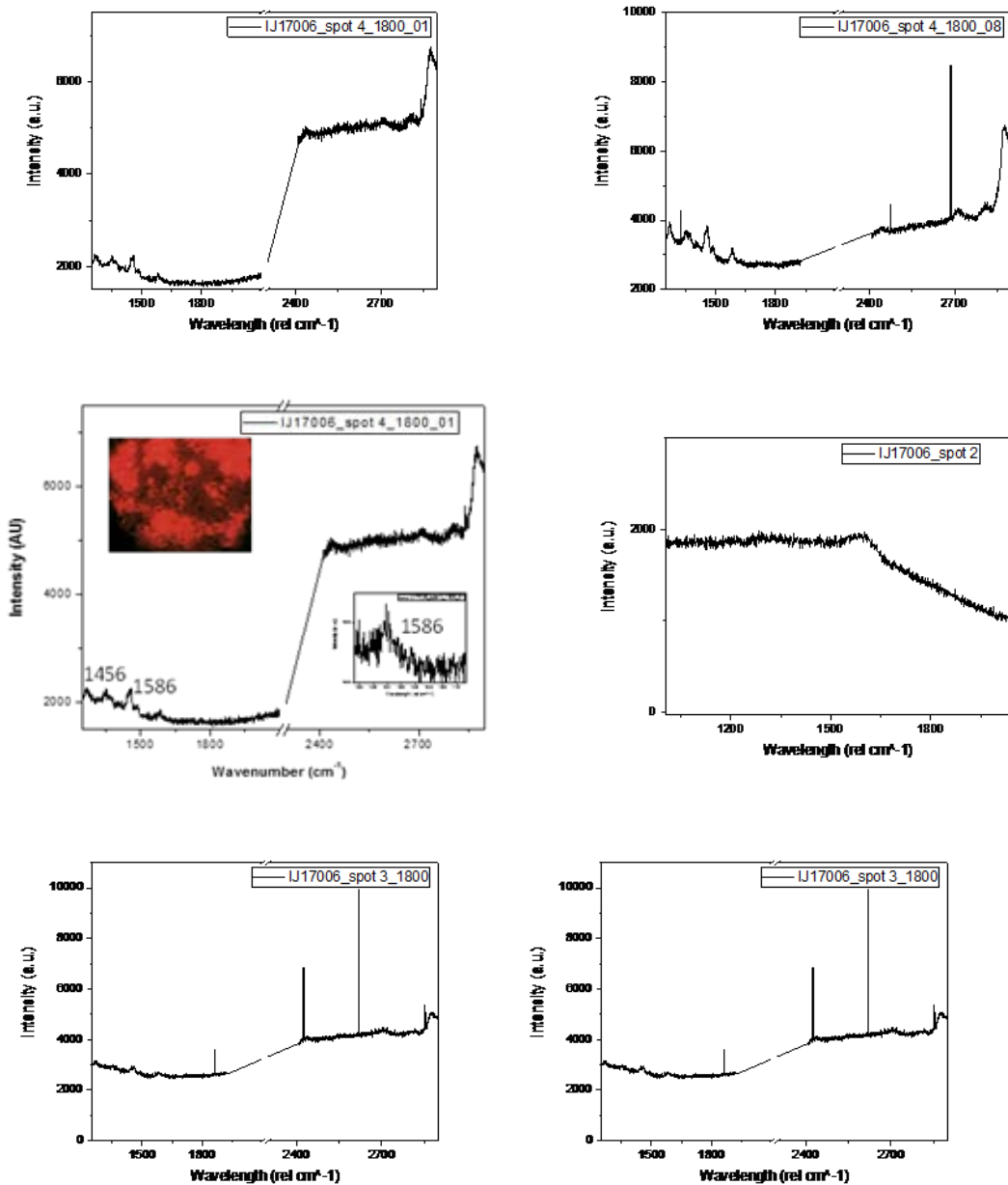


Figure 4.3 shows the Raman Spectra of a sample of graphene ink solution. The expected G-Band peak of pure graphene is a wavenumber of 1580-1590 cm^{-1} .

We plan to complement the design and simulation part of our research with experimental development of a scalable fabrication of graphene on metamaterials. Chemical vapor deposition

(CVD), mechanical exfoliation, chemical exfoliation and chemical synthesis are all methods that have been used for fabrication of graphene on a smaller scale [38]. We will evaluate methods that can be scalable to large areas. For example, graphene printing has been introduced as an alternative fabrication technique for producing graphene that does not have the same high temperature annealing processes as CVD [37][39][41]. Graphene printing is also a low-cost, viable technique that allows for the production of micropatternable graphene films. There are a variety of ways to create graphene ink, including commonly utilized techniques such as liquid-phase exfoliation and shear exfoliation. The disadvantages of these techniques are, despite the fact that they are much more scalable methods than CVD or mechanical exfoliation, a significant amount of graphite remains unexfoliated after the procedures [41]. Additionally, sonication processes can take a considerable amount of time, even after utilizing expensive sonicator tips.

While the method of fabrication for graphene may be liable to change, we feel that graphene printing is the best option because of the importance of large scalability. Graphene ink can be bought commercially from a company or made by a variety of processes. A novel technique called microfluidization has seemed to hold the most promise from recent literature for producing scalable graphene layers [27].

The process of exfoliation of graphite involves the weakening the Van der Waal bonds that hold the layers of graphene together in graphite, without disturbing the covalent bonds within the honeycomb lattice of the graphene layers. To do this, an organic solvent is first used to weaken the Van der Waal bonds [38]. A solution of graphite and solvent begins in an inlet reservoir. A large pressure generated from an intensifier pump is then applied to the solution causing the liquid to be pulled into a channel less than 100 μm in size. This initial step is preferable to the sonication procedures used during liquid-phase exfoliation because a high shear

rate is applied uniformly over the whole liquid, which does not happen during sonication. Once inside the microchambers, the graphite particles collide, creating shear forces that allow for uniform graphene production. The process we plan to develop is illustrated in Figure 4.4.

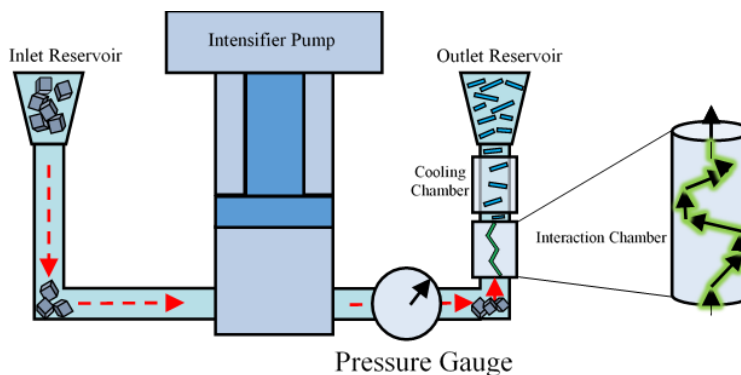


Figure 4.4 Schematic of the envisioned microfluidization process, based on [27].

There have been reports of exfoliation yields as high as 100% [27]. Once the graphene is prepared, they can be mixed into an acrylic polymer binder system in order to gain the proper density, viscosity and surface tension for printing. The graphene ink can then be used in a commercially available inkjet printer for direct printing onto the appropriate, flexible substrate [37].

An important property of graphene, along with its inherently thin structure and flexibility, is its tunable Fermi level, which can be altered by an applied gate voltage [42]. Several different setups have been explored in an effort to alter the absorption, transmission and reflectance of the graphene layers [40][43][44]. These reports will serve as starting points when considering configurations suitable for metamaterials and that can be integrated into solar sails.

One particularly promising approach is to create graphene pattern arrays. The localized plasmon resonances of graphene nanostructures can be exploited to enhance the absorption in

graphene. Since the Fermi level of graphene is controllable through electrostatic doping, the plasmon tunability in infrared can be found depending on the device geometry. Structures such as nanorings, nanoribbons and nanodisks can be used for this purpose [40]. While processes such as e-beam lithography and lift-off procedures would normally be used to create the plasmonic nanostructures, the use of graphene printing could allow for creation of the same structure while simplifying the process considerably. Graphene films will need to be made over a large area on flexible substrates. Since graphene patterning may prove to be the key to producing effective, electrically tunable graphene layers, this technique will be important as we work on this project.

As an alternative to graphene printing, standard microfabrication procedures can also be utilized for graphene patterning. For example, to create disks from graphene, the graphene sheets can be transferred or deposited onto a substrate. The graphene would then be patterned into disk arrays using lithography, with a resist being used to protect the parts of the sample that should not be etched away. Oxygen plasma is used to etch away the exposed area and acetone used to remove the remaining resist. The final result is a disk array such as the one shown in the left image of Figure 4.5 [40]. To complete the proof-of-concept devices, electrodes will be deposited onto the graphene structure through electron beam evaporation. Dielectric layers can be deposited by electron beam evaporation (e.g. SiO_2) or spun on (e.g. polyimide).

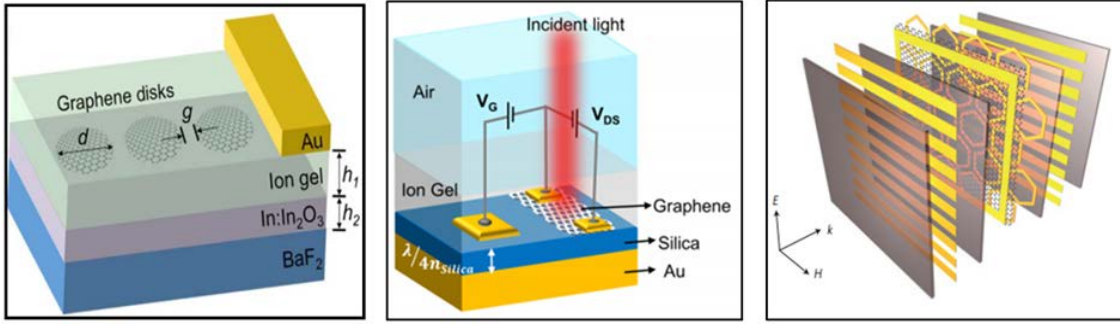


Figure 4.5 Schematics of different setups for optical absorption modification in graphene-based devices. [40][43][44].

Although we will focus on graphene at first, we envision exploring two-dimensional Transition Metal Dichalcogenide (TMDC) materials as well if the need arises. This would be very exploratory and exciting.

We will subsequently characterize the electro-optical properties of the resulting 2D-metamaterial based devices using optical spectrometry, including transmission, reflection and absorption, as well as their electrical tunability. Since the solar sail will primarily be interacting with visible and infrared electromagnetic waves, we will be investigating those regions.

Using an optical broadband source with a large incident illumination spot size, the reflectance R and transmittance T of the arrays of 2D-metamaterial structures can be measured using a Fourier transform spectrometer. The absorbance can then be estimated as

$$A = 1 - R - T. \quad (4.1)$$

Due to the excitation of plasmons associated with free carriers from the array of 2D graphene structures, the Fourier transform infrared spectra should have very prominent resonances. Different values of graphene Fermi energy, E_F , will result in very different resonance amplitudes and positions. The reflectance and absorbance should increase as E_F is changed, while the transmittance should decrease. The Fermi energy of graphene can be found by

applying a top gate bias voltage relative to a lower gate layer. For example, in the case of a nanodisk array, the Fermi energy can be found from

$$E_F = \hbar v_F (\pi n)^{\frac{3}{2}}, \quad (4.2)$$

where the Fermi velocity v_F for graphene is 106 m/s, the carrier density n can be obtained by $n = \frac{c\Delta V}{e}$, and ΔV is found from the I-V characterization measurements [40].

We will compare the results from experimental measurements with our design and simulation predictions as feedback in order to optimize the accuracy of the model and improve the fabrication process if necessary.

One of the main things we needed to consider was the method in which we would fabricate the graphene. It was important that the graphene have large scalability, so for this reason CVD and other techniques could not be used. Graphene printing seems to be a good option because it has large scalability, which is important. The method that was found that seems to be the best option for creating graphene ink is called microfluidization.

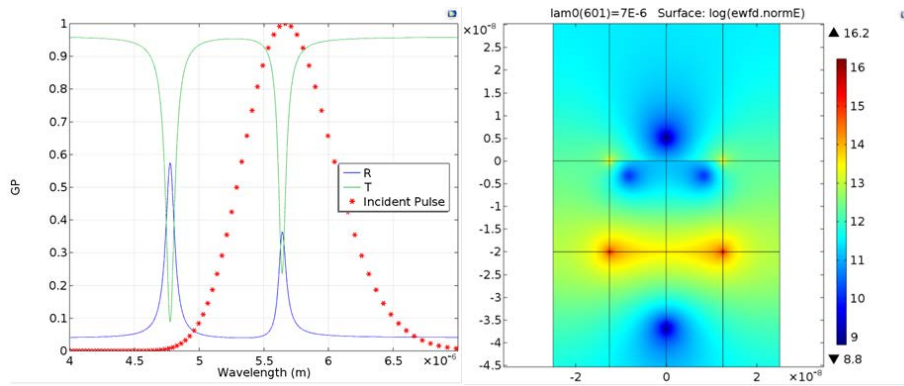


Figure 4.6 (a) Finite element modeling of the optical reflection and transmission of a single layer graphene near 5 μm that I realized using COMSOL Multiphysics. (b) Magnitude of the electric field of the electromagnetic wave as it propagates through the graphene.

A large pressure generated from an intensifier pump is then applied to the solution causing the liquid to be pulled into a channel less than 100 μm in size. A high shear rate is applied uniformly over the whole liquid. Once inside the microchambers, the graphite particles collide, creating shear forces that allow for uniform graphene production. The microfluidization technique allows for most, if not all of the graphite used in the solution to be converted into graphene.

In the future, it will be useful to create additional Finite Element Method (FEM) simulations of graphene sheets, taking into account the thermodynamic, mechanical, optical and electrical properties of the material. The next task is to begin fabricating a device that has potential to tune the reflectivity and absorption of graphene. The microfluidization procedure we mentioned above would be a big part of this. The last task is to characterize the device that we created. We would do IV characterization of the sample, along with time domain spectroscopy in order to examine how the optical reflection and absorption of the sample changes with an applied voltage.

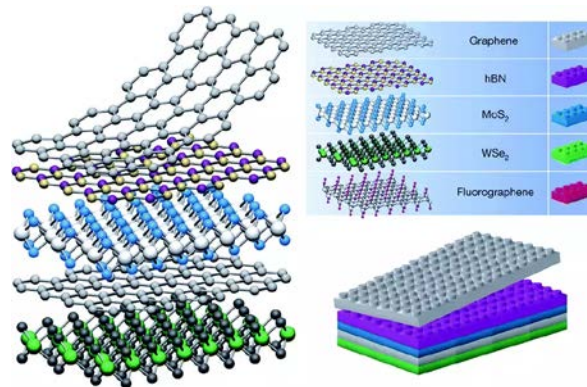


Figure 4.7 Examples of two-dimensional materials. The structures of these materials allows for them to be easily stacked [45].

4.2 Characterization

To describe Raman spectroscopy, it is useful to explain the difference between two different types of scattering processes for photons interacting with molecules. The two scattering processes are Rayleigh and Raman scattering. The first process, Rayleigh scattering, comes about from a photon undergoing elastic scattering with a molecule. The incident photon is absorbed by the molecule, which excites the molecule. The molecule will then emit another photon with the same energy as the original incident photon. Most of all photon-molecule scattering interactions are Rayleigh scattering.

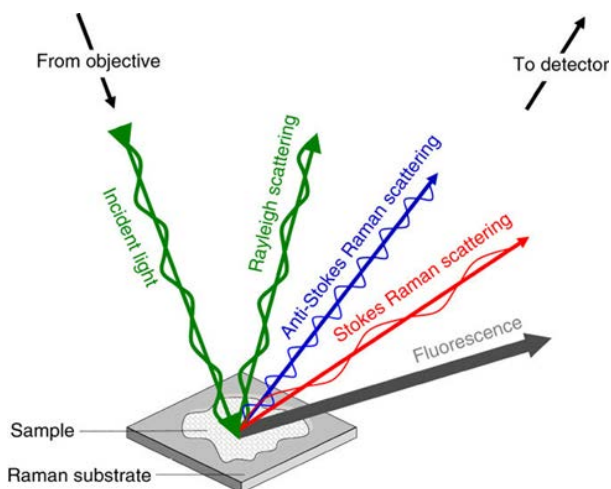


Figure 4.8 Illustration depicting the various scattering phenomena which can occur during the scattering of incident radiation. In Raman spectroscopy, the measured scattering are from the Stokes and Anti-Stokes Raman scattering [31].

During Raman scattering, on the other hand, the photons will undergo inelastic scattering with the molecules, which means that they will lose or gain energy as they interact, and a photon of different energy and frequency will be emitted. As mentioned before, very small percentage of

photon-molecule scattering interactions are Raman scattering, with the vast majority of scattering being Rayleigh scattering.

In addition to elastic and inelastic scattering, there are two additional subcategories of inelastic scattering, which can both also be referred to as Raman scattering. The first one, called anti-Stokes scattering, is where the released photon from the inelastic collision of the incident photon with a molecule, create a photon with a higher energy than the original incident photon. This can occur because the electric field of the incident light wave interacts constructively with the induced electric dipole of the molecule. In that case, the change in photon energy is equal to the change in vibrational energy of the molecule.

The other type of inelastic scattering is called Stokes scattering, and undergoes the opposite process. While the photon that underwent anti-Stokes scattering was reemitted at a higher energy level, the photon in this case will be reemitted at a lower energy level. This is due to destructive interference of the induced electric dipole from incident radiation. Most of the time when Raman scattering occurs, the scattered photon will have a lower energy and frequency than the incident photon, so Stokes scattering is more prominent in relation to anti-Stokes scattering. Like anti-Stokes scattering, the change in energy from the original incident photon from the emitted photon can be equal to the change in vibrational energy of the molecule, or even the collective system of molecules, which is also called a phonon. A phonon is the collective excitation in a periodic arrangement of molecules in a solid, and it is representative of the different vibrational mode excited states for the system. In both Stokes and anti-Stokes scattering, a phonon can be released from the interaction of the molecule with the original incident photon.

Raman spectroscopy was developed from the collective work of Adolf Smekal and C.V. Raman. In 1923, Smekal theoretically discovered the existence of inelastic scattering. At the same time, C.V. Raman was also investigating diffraction of light, which led to him experimentally discovering Raman scattering in 1928. The efforts of these two physicist gave rise to the characterization technique, Raman spectroscopy, and in 1930, C.V. Raman received a Nobel Prize for his work.

Raman spectroscopy is the measurement of the molecular vibrations of the molecules using a laser. The basic method to perform Raman spectroscopy is to first use a monochromatic light source to radiate the sample that is being investigated. A spectrometer is used to measure the intensity of the light as a function of the wavenumber. Most of the photons from the laser will be elastically scattered, but a small amount of them will be inelastically scattered, which will be the photons of interest. Raman scattering is a relatively weak phenomenon, so filters must be used to filter out the radiation from Rayleigh scattering. Modern Raman spectroscopy setups typically used notch or edge filters, but in the past photomultipliers were also utilized to increase the signal strength of the Raman scattering. After the Raman scattering is separated from the Rayleigh scattering, it is then possible to measure the difference between the photon energy between the inelastically scattered photons and the original incident photons to get a measurement of the vibrational mode of the molecule or system. A Raman spectrum is a plot of the intensity of the Raman scattered radiation as a function of the energy difference from the incident radiation (usually expressed as a function of wavenumber because of the relationship between energy and wavelength). In addition to finding the vibrational modes, Raman scattering can also give insight into other low energy excited states, such as rotational modes.

Because the vibrational modes of a molecule or a system of molecules will be different depending on the material, the Raman spectrum can be thought of as a type of fingerprint for the sample that is being measured. This means that in any situation where it is important to know exactly what substance is present in a given sample, Raman spectroscopy can probably be utilized. Some examples of applications of Raman spectroscopy include investigation of quality and number of layers in graphene, mineral identification in geology, chemical analysis of pharmaceutical and cosmetic products, and characterization of semiconductors (including defect analysis and superlattice structure).

Raman scattering is a commonly used and important characterization technique for many reasons. One important benefit of Raman spectroscopy is that it is nondestructive to the sample. This, in addition to the fact that it is a relatively quick and easy method to obtain both qualitative and quantitative measurements of a sample, makes Raman scattering a very useful tool for scientists and engineers to obtain information on the chemical properties of a material.

CHAPTER 5. FUTURE RESEARCH PLANS

The primary objective of this research is to create a method of generating lateral forces, which could be used to create a torque along the roll axis of the sail. Furthermore, the new method must be able to meet current mission specifications. Since the NEA Scout mission targeted launch date is in 2019, we will primarily be comparing the results from our research to the current literature pertaining to the NEA Scout mission.

Another important objective will be to demonstrate that the proposed metasurface allows for full controllability of the solar sail attitude. While a demonstration that the metasurface can create the desired lateral forces from its interaction with oncoming Electromagnetic (EM) radiation will be great, it will be useless unless there is also an effective method to turn on and off the anomalous reflections. For the situations where a torque along the roll axis is no longer required, electric dipoles along the metasurface can be induced to nullify the phase gradient of the metasurface and remove the component of the reflected wavevector that is tangential to the incident wavevector. This would effectively return Snell's law of reflection to its more familiar form in which $\theta_i = \theta_r$. The electric dipoles can be activated by the application of a bias voltage to the metasurface, and would return the metasurface to a specularly reflecting mirror. This would eliminate the lateral forces. From here, light would create exclusively normal forces, and previously developed technology could be utilized to further control this parameter (such as the reflectivity control devices that were used on the surface of the IKAROS solar sail). For these reasons, it will be important to analyze the effect of an electric dipole on the metasurface and be

sure the simulations and experimental data support the idea that the anomalous reflections can be turned off. An alternative (or additional) option to consider is to integrate an ultrathin layer of liquid crystals on top of our proposed ARM devices. The liquid crystals have been shown to be able to exhibit a controllable opacity, so this additional layer could act as a barrier layer to cover the metasurface when the anomalously reflection forces are not required.

An additional objective that is slightly lower priority is to implement a fabrication method that could be utilized in further development/manufacturing of solar sail metasurfaces. It is a low priority only because it would be possible to provide proof-of-principle evidence of the metasurfaces working without realizing the kind of large-scale manufacturing that would be necessary to cover a modern solar sail. The method and scalability of the fabrication of the metasurface depends upon the final metasurface design and material.

The final future objective is to characterize the final fabricated metasurface and demonstrate that anomalous reflections have been achieved. Furthermore, we will show that the anomalous reflections are able to exhibit real life reflection forces, which would be sufficient to generate a torque along the roll axis. We will show that the metasurfaces are electrically controllable, and that an applied bias voltage to the metasurfaces does induce the desired specular behavior.

5.1 Designing and Modeling of ARM

The first step to designing a metasurface with the proper phase gradient to allow for anomalous reflection is fully developing the mathematical background behind this phenomenon through modeling. Building on the underlying scientific principles discussed previously, we will carry out multi-physics FEM and confirmed by finite-difference time-domain (FDTD) modeling on a few simple designs of metasurfaces. Gradually, we will increase the complexity of the

design to optimize efficiency, phase gradient response, functional bandwidth as well as integrating the effect of the angle of incidence of the sun light. This will be done in parallel to experimental fabrication and measurements to gain better access to actual physical quantities.

Specifically, the design and modeling work builds on our experience gained when we were developing the three-dimensional multiphysics FEM of a few metamaterials and using it to model their interaction with electromagnetic waves. In that preliminary work, these models have allowed us to extract the propagation characteristics of the wave, in terms of propagation direction, polarization and magnitude.

At a later stage in the project, we plan to integrate mechanical aspects of the metasurfaces-on-sail membranes and determine the impact on the metasurface optical properties. Experimental measurements will be compared with the analytical model predictions to refine the model as well as optimize the fabrication process.

While we have already obtained results showing a resultant torque along the roll axis of the solar sail when using a constant phase gradient anomalously reflecting metasurface, there may be a better solution. The constant phase gradient metasurfaces can produce the required magnitude of torque along the roll axis of the sail, but there is also a large dependence on the incident angle of the incoming electromagnetic wave. An ideal anomalously reflecting metasurface would exhibit a uniform torque for all angles of incidence.

5.2 Demonstration of Anomalous Reflection Force

Based on the findings from the design and modeling task, we will concurrently carry out the fabrication of such metasurfaces on flexible polyimide or mylar membranes that are compatible with solar sail membranes. To do so, we will use the expertise and processes

established in our group for the realization of other metamaterials on polyimide, including mask design, lithography and metal evaporation followed by lift-off.

The light reflection characteristics of the fabricated metasurfaces will be measured to confirm the relationship between incident and reflection angles, as well as associated efficiencies. We will also continue to optimize the metasurfaces to further enhance the efficiency of the anomalous reflection of light. These measurements will provide experimental values that we will in turn use to refine our models.

The fabrication technique that we will use for small-scale demonstrations of lateral forces due to radiation pressure will vary depending on the metasurface that is being tested. Since the best option currently under consideration is one that exhibits a constant phase gradient, the fabrication method best suited to these types of structures will be discussed.

The metasurface array that we had primarily focused on while deriving the forces on the solar sail from anomalous reflections, was an array of rectangular golden slabs of equal thickness. The width of the slabs increases for every other slab, until it reaches a maximum width. The length of one unit cell of these gradient metamaterials, from minimum to maximum width, is denoted l , which is the length of the unit cell. An array of these unitcells make up the considered metasurface, and exhibits a constant phase gradient [18][21][46].

The next priority will be to characterize the fabricated metasurfaces. There are a few properties that will be of particular importance, such as the reflectivity and the force created from an illumination source. To measure reflection, absorption and transmission, we will use a Fourier Transform spectrometer available within the lab of our research group. Additionally, characterization techniques that can be used to determine the force from optical waves include using interferometric techniques and an atomic force microscope [47][48].

5.3 Investigation of Integration on Solar Sail

In this task, we will study the impact of ARM on the attitude of the solar sail using FEM simulation, especially roll. The work will take as input parameter the shape of the sail (curvature) as well as placement/orientation/size of the metasurfaces on the sail. At first approximation, we anticipate that the placement of such structures would theoretically be made in a configuration such as the one in Figure 5.1.

To help with this part of the proposed work, we have carried out some preliminary modeling of the sail dynamics (without metasurfaces for now), based on mathematical formalism. The outcome from our simulations includes the total force and torque based on incident light and angle, as well as the mechanical properties of the sail such as its curvature. The ultimate goal of this thesis will be to create a final design that will be utilized for the next stage of technological development of the ARM devices, namely fabrication and prototyping.

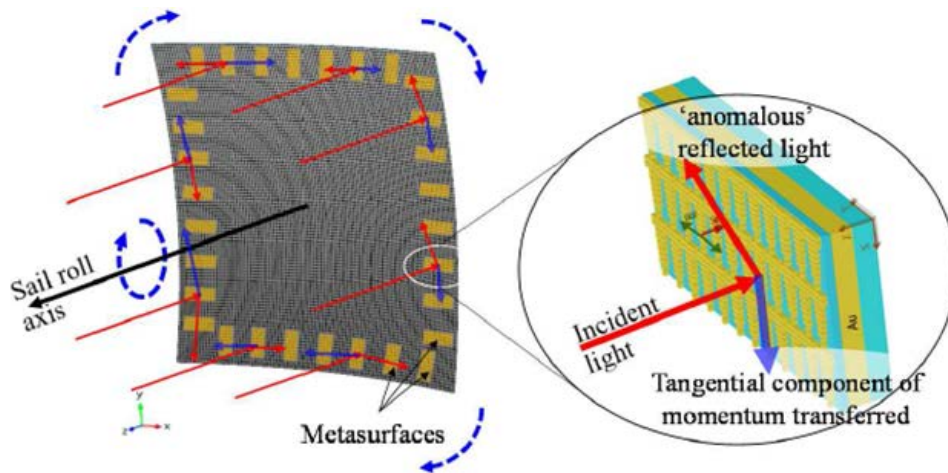


Figure 5.1 Illustration of metasurfaces on a solar sail, resulting in in-plane tangential forces as a result of anomalous reflection of light.

CHAPTER 6. CONCLUSION

The analysis work that has been carried out to this point provides a clear picture of the different attitude control properties that can be expected from utilizing different materials to tune the reflecting properties of the solar sail surface. The one that has shown perhaps the most promise for offering effective, novel means for attitude management is the integration of metamaterial surfaces. The anomalous reflection forces and torque that have been derived show that an increased torque can be exhibited, even along the roll axis, which has been an area of difficulty for prior propellant-free systems. With the utilization of phase gradients of opposing signs, the torque on the solar sail can be made symmetric for positive and negative angles of incidence.

Reflection control devices also offer an effective means of attitude control, which has been explored mathematically. While torques along the roll axis are not achieved to the same effectiveness as the cases involving the anomalously reflecting metasurfaces, RCDs are a good option for creating torque along the other principle axes.

A possible option for future implementation of ARM or RCD technology could be to utilize a combination of options. If RCD could be made to switch from perfectly reflecting to perfectly transmitting, they could act as a barrier for metasurfaces housed beneath them when they are not in operation. Another option could be to explore potential methods of electrically tuning the reflection properties of the metamaterial surfaces by inducing an electric dipole by biasing the metamaterial structure.

Regardless of the future methods of tuning the attitude control technology on the solar sail systems, it has been shown from our analysis that a phase gradient of $0.71k_0$ is an optimal magnitude phase gradient to achieve high torques along the roll axis. Conversely, very small, nonzero phase gradients exhibit the most gradual variation of torque over the full range of incidence angles. These design parameters will be important when choosing metamaterial structure dimensions that support future space mission parameters. For the case of RCDs, the highest magnitude torque is created from the largest difference in optical coefficients, whether it is from switching between perfect specular reflections to perfect diffuse reflections, or from perfect reflection to perfect transmission.

Upon comparison with the force and torque plots from current reflection control devices such as those that were utilized on IKAROS, the anomalously reflecting metasurfaces offer a considerable increase in torque along the roll axis. This is important because up until this point, roll control has been a particularly difficult aspect of solar sail attitude control to manipulate without the use of reaction wheels or propellant. The torque along the roll axis can reach values of torque as high as $358 \mu N m$ under ideal conditions, while no roll torque can be achieved by varying the specular reflectivity of the reflection control devices from specular to diffuse.

One thing that is important to note, is that for the force plots of the anomalously reflecting metasurfaces, there was a point where the normal force switches signs, and is acting in the opposite direction of the normal component of the incident wavevector. It is doubtful that this situation would lead to an attractive force (i.e. force pulling the sail towards the light). It is more likely that at the incident angles where the negative force is created, the propagating waves would convert into localized surface plasmons, which would require different mathematical treatment to characterize.

This work demonstrates the importance of considering the manipulation of the optical properties of solar sails for attitude control, and the positive outlook for the realization of future solar sails with completely propellant-free attitude control with no additional mechanical actuators to add mass to the system.

REFERENCES

- [1] Macdonald, M. (Ed.). (2014). *Advances in solar sailing*. Springer Science & Business Media.
- [2] A. Pors, O. Albrektsen, I. P. Radko and S. I. Bozhevolnyi, "Gap plasmon-based metasurfaces for total control of reflected light," *Scientific reports*, vol. 3, 2013.
- [3] N. Yu, P. Genevet, M. A. Kats, F. Aieta, J.-P. Tetienne, F. Capasso and Z. Gaburro, "Light propagation with phase discontinuities: Generalized laws of reflection and refraction," *Science (New York, N.Y.)*, vol. 334, no. 6054, p. 333–337, 2011.
- [4] H.-X. Xu, S. Tang, S. Ma, W. Luo, T. Cai, S. Sun, Q. He and L. Zhou, "Tunable microwave metasurfaces for high-performance operations: Dispersion compensation and dynamical switch," *Scientific reports*, vol. 6, 2016.
- [5] Y. Tsuda, "How IKAROS Shape is Designed: Attitude Stability of Spinning Solar Sail," in Macdonald (Ed.) – *Advances in Solar Sailing*, Springer, Berlin, Heidelberg, 2014, p. 45–56.
- [6] O. Mori, Y. Shirasawa, Y. Mimasu, Y. Tsuda, H. Sawada, T. Saiki, T. Yamamoto, K. Yonekura, H. Hoshino, J. Kawaguchi and R. Funase, "Overview of IKAROS Mission," in Macdonald (Ed.) – *Advances in Solar Sailing*, Springer, Berlin, Heidelberg, 2014, p. 25–43.
- [7] Y. Shirasawa, O. Mori, N. Okuizumi, Y. Satou, A. Yamasaki, H. Furuya, T. Nishizawa, H. Sakamoto and G. Ono, "Evaluation of Sail Mechanics of IKAROS on its Slow-Spin and Reverse-Spin Operation," in Macdonald (Ed.) – *Advances in Solar Sailing*, Springer, Berlin, Heidelberg, 2014, pp. 55-74.
- [8] A. F. Heaton, B. F. Faller and C. K. Katan, "NanoSail:D Orbital and Attitude Dynamics," in Macdonald (Ed.) – *Advances in Solar Sailing*, Springer Berlin Heidelberg, 2014, p. 95–113.
- [9] S. Sun, K.-Y. Yang, W. Chen, C. Liao, G. Guo, D. Tsai, C. Wang, T. Juan, W.-T. Kung and Q. He, "Highly efficient anomalous reflection by an optical metasurface," *SPIE Newsroom*, 2013.
- [10] McInnes, Colin R. *Solar sailing: technology, dynamics and mission applications*. Springer Science & Business Media, 2013.
- [11] Fu, B., Sperber, E., & Eke, F. (2016). Solar sail technology—a state of the art review. *Progress in Aerospace Sciences*, 86, 1-19.
- [12] A. Heaton, N. Ahmad and K. Miller, "Near Earth Asteroid Scout Solar Sail Thrust and Torque Model," in 4th International Symposium on Solar Sailing, Kyoto, 2017.

- [13] A. C. D. Walden and L. Johnson, "Near-Earth Asteroid Scout," George C. Marshall Space Flight Center Research and Technology Report 2014, Huntsville, 2015.
- [14] R. Ridenoure, R. Munakata, Wong, S.D., A. Diaz, D. Spencer, D. Stetson, B. Betts, B. Plante, J. Foley and J. Bellardo, "Testing The LightSail Program: Advancing Solar Sailing Technology Using a CubeSat Platform," *Journal of Small Satellites*, vol. 5, no. 2, pp. 531-550, 2016.
- [15] K. Achouri and C. Caloz, "Metasurface Solar Sail for flexible Radiation Pressure Control," *ArXiv e-prints*, vol. 1710, 2017.
- [16] E. J. Rothwell and M. J. Cloud, *Electromagnetics*, Boca Raton: CRC Press, 2008.
- [17] J. P. Barton, D. R. Alexander and S. A. Schaub, "Theoretical determination of net radiation force and torque for a spherical particle illuminated by a focused laser beam," *Journal of Applied Physics*, vol. 66, no. 10, pp. 4594-4602, 1989.
- [18] S. Sun, K.-Y. Yang, C.-M. Wang, T.-K. Juan, W. T. Chen, C. Y. Liao, Q. He, S. Xiao, W.-T. Kung, G.-Y. Guo, L. Zhou and D. P. Tsai, "High-Efficiency Broadband Anomalous Reflection by Gradient Meta-Surfaces," *Nano Letters*, vol. 12, no. 12, pp. 6223-6229, 2012.
- [19] S. Orfanidis, *Electromagnetic Waves and Antennas*, Piscataway: Rutgers University, 2016.
- [20] D. Staelin, *Electromagnetics and Applications*, Cambridge: Massachusetts Institute of Technology, 2011.
- [21] Y. Z. Ho, B. H. Cheng, W.-L. Hsu, C.-M. Wang and D. P. Tsai, "Anomalous reflection from metasurfaces with gradient phase distribution below 2π ," *Appl. Phys. Express (Applied Physics Express)*, vol. 9, no. 7, 2016.
- [22] Geng, Y., Tan, J., Cao, Y., Zhao, Y., Liu, Z., & Ding, W. (2018). Giant and tunable optical torque for micro-motors by increased force arm and resonantly enhanced force. *Scientific reports*, 8(1), 2819.
- [23] Z. Zhu, I. Murtaza, H. Meng, and W. Huang, "Thin film transistors based on two dimensional graphene and graphene/semiconductor heterojunctions," *RSC Advances*, vol. 7, no. 28, pp. 17387-17397, 2017.
- [24] A. Jana, E. Scheer, and S. Polarz, "Synthesis of graphene-transition metal oxide hybrid nanoparticles and their application in various fields," *Beilstein Journal of Nanotechnology*, vol. 8, pp. 688-714, 2017.
- [25] M. Silberberg, *Chemistry: The Molecular Nature of Matter and Change With Advanced Topics*. McGraw-Hill, 2018.
- [26] F. Bonaccorso and Z. Sun, *Solution processing of graphene, topological insulators and other 2d crystals for ultrafast photonics*. 2014.
- [27] P. G. Karagiannidis, S. A. Hodge, L. Lombardi, F. Tomarchio, N. Decorde, S. Milana, I. Goykhman, Y. Su, S. V. Mesite and D. N. Johnstone, "Microfluidization of graphite and formulation of graphene-based conductive inks," *ACS nano*, vol. 11, no. 3, pp. 2742-2755, 2017.

- [28] B. Yadav, R. Kumar, R. Srivastava, and T. Shukla, Flame Synthesis of Carbon Nanotubes using Camphor and its Characterization. 2011.
- [29] C. Wong, C. Lai, K. Lee, and S. Hamid, "Advanced Chemical Reduction of Reduced Graphene Oxide and Its Photocatalytic Activity in Degrading Reactive Black 5," *Materials*, vol. 8, no. 10, p. 5363, 2015.
- [30] P. Deka, Large-Area Graphene oxide membranes for water purification 1 fabrication of large-area liquid crystal graphene oxide membrane by shear alignment method (sam) large-area graphene oxide membranes for water purification 2. 2017.
- [31] H. J. Butler et al., "Using Raman spectroscopy to characterize biological materials," *Nature Protocols*, vol. 11, p. 664, 03/10/online 2016.
- [32] C. Lee, X. Wei, J. W. Kysar and J. Hone, "Measurement of the elastic properties and intrinsic strength of monolayer graphene," *Science*, vol. 321, no. 5887, pp. 385-388, 2008.
- [33] A. K. Geim and K. S. Novoselov, "The rise of graphene," *Nature materials*, vol. 6, no. 3, p. 183, 2007.
- [34] P. Delhaes, Graphite and precursors, vol. 1, CRC Press, 2000.
- [35] H. Boehm, A. Clauss, G. Fischer and U. Hofmann, "Surface properties of extremely thin graphite lamellae," in *Proceedings of the fifth conference on carbon*, 1962.
- [36] K. S. Novoselov, A. K. Geim, S. V. Morozov, D. Jiang, Y. Zhang, S. V. Dubonos, I. V. Grigorieva and A. A. Firsov, "Electric field effect in atomically thin carbon films," *Science*, vol. 306, no. 5696, pp. 666-669, 2004.
- [37] I. Banerjee, T. Faris, Z. Stoeva, P. G. Harris, J. Chen, A. K. Sharma and A. K. Ray, "Graphene films printable on flexible substrates for sensor applications," *2D Materials*, vol. 4, no. 1, p. 015036, 2016.
- [38] M. S. A. Bhuyan, M. N. Uddin, M. M. Islam, F. A. Bipasha and S. S. Hossain, "Synthesis of graphene," *International Nano Letters*, vol. 6, no. 2, pp. 65-83, 2016.
- [39] R. D. Farahani, M. Dubé and D. Therriault, "Three-dimensional printing of multifunctional nanocomposites: manufacturing techniques and applications," *Advanced Materials*, vol. 28, no. 28, pp. 5794-5821, 2016.
- [40] Z. Fang, Y. Wang, A. E. Schlather, Z. Liu, P. M. Ajayan, F. J. García de Abajo, P. Nordlander, X. Zhu and N. J. Halas, "Active tunable absorption enhancement with graphene nanodisk arrays," *Nano letters*, vol. 14, no. 1, pp. 299-304, 2013.
- [41] S. Majee, M. Song, S.-L. Zhang and Z.-B. Zhang, "Scalable inkjet printing of shear-exfoliated graphene transparent conductive films," *Carbon*, vol. 102, pp. 51-57, 2016.
- [42] J. Linder and K. Halterman, "Dynamical tuning between nearly perfect reflection, absorption, and transmission of light via graphene/dielectric structures," *Scientific reports*, vol. 6, p. 38141, 2016.

- [43] S. H. Lee, M. Choi, T.-T. Kim, S. Lee, M. Liu, X. Yin, H. K. Choi, S. S. Lee, C.-G. Choi and S.-Y. Choi, "Switching terahertz waves with gate-controlled active graphene metamaterials," *Nature materials*, vol. 11, no. 11, p. 936, 2012.
- [44] V. Thareja, J.-H. Kang, H. Yuan, K. M. Milaninia, H. Y. Hwang, Y. Cui, P. G. Kik and M. L. Brongersma, "Electrically tunable coherent optical absorption in graphene with ion gel," *Nano letters*, vol. 15, no. 3, pp. 1570-1576, 2015.
- [45] Geim, A. K., & Grigorieva, I. V. (2013). Van der Waals heterostructures. *Nature*, 499(7459), 419.
- [46] H. Zhu, X. Yin, L. Chen and X. Li, "Directional beaming of light from a subwavelength metal slit with phase-gradient metasurfaces," *Scientific reports*, vol. 7, no. 1, 2017.
- [47] G. Meyer and N. M. Amer, "Simultaneous measurement of lateral and normal forces with an optical-beam-deflection atomic force microscope," *Applied physics letters*, vol. 57, no. 20, pp. 2089-2091, 1990.
- [48] S. Fujisawa, M. Ohta, T. Konishi, Y. Sugawara and S. Morita, "Difference between the forces measured by an optical lever deflection and by an optical interferometer in an atomic force microscope," *Review of scientific instruments*, vol. 65, no. 3, pp. 644-647, 1994.